Time-Domain-Optimized Antenna Array for High-Precision IR-UWB Localization in Harsh Urban Shipping Environments

Gert-Jan Gordebeke, *Member, IEEE,* Sam Lemey, *Member, IEEE,* Olivier Caytan, *Member, IEEE,* Michiel Boes, Jelle Jocqué, Samuel Van de Velde, Chris Marshall, Eli De Poorter and Hendrik Rogier, *Senior Member, IEEE*

***Abstract*— Urban freight distribution via inland waterways is an important way to boost the quality of life in major urban areas with dense water networks. Cost-effective autonomous pallet shuttle barges (PSBs) are key to accelerate the shift from road-based transport to inland waterways. Yet, the urban settings impede reliable centimeter-level localization at critical waterway sections. In this article, we propose a time-domain-optimized antenna array to provide high-precision 3D localization in these complex environments with minimal shore-side infrastructure by exploiting impulse-radio ultra-wideband (IR-UWB) technology. To enable joint distance and 2D angle-of-arrival (AoA) estimation, we present a novel IR-UWB antenna element that covers channels 5 and 7 of the IEEE 802.15.4z standard, serving as a building block for scalable multi-antenna systems. By leveraging the air-filled substrate-integrated-waveguide technology and adopting a multi-objective system-level optimization strategy, excellent performance is reconciled with a compact footprint and cost-effective fabrication. The 3D positioning accuracy of a 2 × 2 array is evaluated in stand-alone conditions and when installed on a metal plate mimicking a PSB's metal hull, showing that all distance errors and 97 % of angular errors remain below 2 cm and 5°, respectively. Finally, three anchor nodes, each consisting of a 1 × 4 array connected to a Pozyx hardware platform, are installed on a vessel navigating in a narrow canal below a bridge in Ghent. With only one shore-side UWB beacon node deployed, 96 % of AoA estimation errors remain below 10°, while the distance error remains below 10 cm, proving good installed performance in harsh urban shipping environments.**

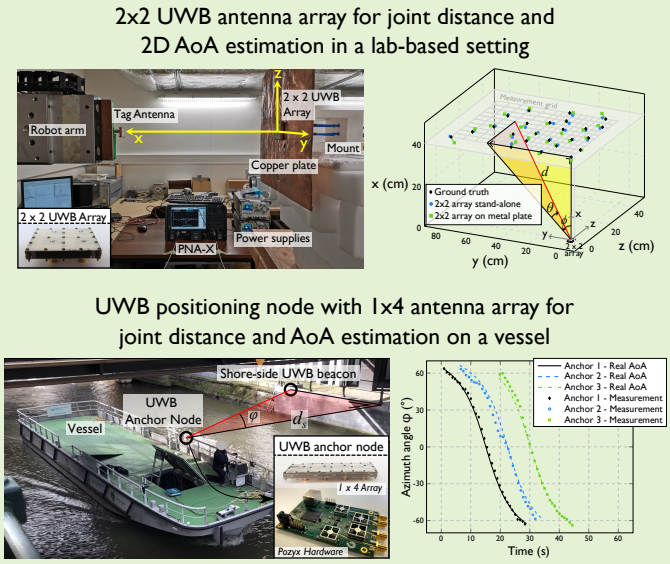

***Index Terms*— Air-filled substrate-integrated-waveguide (AFSIW), angle-of-arrival (AoA), cavity-backed slot antenna, impulse-radio ultra-wideband (IR-UWB), localization, time-domain optimization, urban shipping.**

I. Introduction

ADVANCED intelligent transport systems (ITSs) are vital to optimize mobility in the Smart City of the future [1]. They can make transport safer [2], more efficient and more sustainable [3] by applying the rapid advancement in information and wireless communication technologies to all modes of passenger and freight transport [4], [5]. In cities with dense water networks, there has been a strong focus on moving the last-mile logistics (LML) to local waterways to ensure higher-volume cargo flows to end consumers, while boosting the quality of life in the city center by lowering road congestions and reducing greenhouse gas emissions [6], [7]. To accelerate this modal shift, cost-effective autonomous pallet shuttle barges (PSBs) are of key importance [8].

Over the last few years, significant research efforts have accelerated the development of autonomous surface vehicles (ASVs) [9], such as the improvement of motion-control and path-planning algorithms focusing on safety and environmen-

Manuscript received Month ??, 2023; revised Month ??, 2023; accepted Month ??, 2023. Date of publication Month ??, 2023; date of current version August 23, 2023. This research was partially funded by the imec.icon SmartWaterWay project. (*Corresponding author: Gert-Jan Gordebeke.*)

Gert-Jan Gordebeke, Sam Lemey, Olivier Caytan, Jelle Jocqué, Eli De Poorter and Hendrik Rogier are with the Department of Information Technology, Ghent University/imec, 9052 Ghent, Belgium (e-mail: gertjan.gordebeke@ugent.be).

Samuel Van de Velde and Michiel Boes are with Pozyx, 9000 Ghent, Belgium (e-mail: samuel@pozyx.io).

Chris Marshall is with imec Netherlands, 5656 AE Eindhoven, The Netherlands (e-mail: chris.marshall@imec.nl).

Digital Object Identifier ??

tal dynamics in maritime scenarios [10], collision-avoidance navigation systems [11] and coordinated control methods for fleets of ASVs [12]. However, current ASVs rely heavily on expensive sensor setups, combining real-time kinematic global navigation satellite system (RTK-GNSS) data with data obtained from inertial measurement/navigation systems, high-end 360° electro-optical, infrared or thermal cameras and radio detection and ranging (RADAR) [13] or light detection and ranging (LIDAR) hardware [14]–[16], to ensure reliable autonomous navigation in maritime and harbor settings.

While for larger vessels, the sensor cost is negligible compared to the cost of the ship itself, it impedes the economic viability of smaller PSBs, hindering their large-scale roll-out [8], [17]. Moreover, GNSS-based positioning in urban environments is greatly challenged by notorious multipath effects and non-line-of-sight conditions [18], due to bridges and high-rise buildings [19]. In particular, for narrow inland waterways in an urban setting and for harbors, which are highly dynamic environments, this can result in navigation failure at critical locations [20], such as blind spots (turns, forks, bridges), loading/unloading docks and locks [16], [21]. Additionally, to enable self-docking and self-(un)loading, docks and locks require centimeter-precision 3D positioning of the vessel to also accurately determine its height with respect to the shore [20]–[22].

To provide reliable and high-accuracy 3D position information in these complex scenarios in a cost-effective way, an impulse-radio ultra-wideband (IR-UWB) system can be deployed at the critical waterway sections, while the vessel can rely on standard GNSS-based navigation during the remaining, and largest part, of its trajectory. IR-UWB has emerged as the prime candidate for localization systems deployed in GNSS-denied environments, mostly in indoor positioning systems [23], [24], but more recently also in outdoor settings [20], [25], [26], owing to its high (centimeter-level) accuracy and resilience against multipath and narrowband interference. Furthermore, it allows for coexistence with other wireless technologies, a major advantage in combined localization, communication and sensing platforms, such as autonomous vessels [20], [23]. However, UWB localization systems typically use single-antenna devices and leverage either time-of-arrival (ToA) estimation, two-way-ranging (TWR), or time-difference-of-arrival (TDoA) estimation schemes [27]–[29] for robust and accurate positioning, requiring several (cabled) anchor nodes at fixed infrastructure locations. For urban shipping, such an approach would lead to an excessive amount of shore-side infrastructure.

By adopting multi-antenna UWB nodes, the number of infrastructure nodes and the associated installation cost can be significantly reduced, while further improving localization accuracy by leveraging the phases and/or arrival times at each of the antenna elements to implement joint distance and angle-of-arrival (AoA) estimation [24], [30], [31]. The surge in popularity of multi-antenna nodes is evidenced by the abundance of UWB AoA or hybrid ToA/AoA localization algorithms [32]–[34] proposed in recent years. The phase-difference-of-arrival (PDoA) technique [35]–[38] is of particular interest owing to its (computational) simplicity and scalability to larger multi-antenna nodes, while still providing accurate angular information.

In contrast to the rapid development of localization algorithms exploiting multi-antenna nodes, dedicated multi-antenna IR-UWB systems for joint distance and 2D AoA estimation are scarcely available. This is because it is extremely challenging to achieve a large bandwidth in a low-profile and compact antenna footprint, as needed to realize planar $\lambda/2$-spaced antenna arrays with low mutual coupling and hemispherical radiation for unambiguous 2D PDoA-based AoA estimation [35]. In addition, their design is further complicated as IR-UWB applications require thorough antenna optimization in the frequency and time domain, both at element and system level, to minimize orientation-specific pulse distortion, group delay variation and phase center variation [39]–[42]. Moreover, for mass deployment in challenging environments [23], [43], [44], such as integration in the hull of (autonomous) vessels, the multi-antenna IR-UWB hardware should be compatible with standard manufacturing technologies and facilitate compact integration with ICs and active electronics, to reduce overall system cost and size. At the same time, the antenna elements should exhibit maximal robustness against their environment and integration platform, which, on vessels, consists predominantly of metal. This is of major importance, as undesired electromagnetic coupling with the integration platform, such as a human body or vessel [45], [46], causes antenna detuning, radiation pattern deformation and severely reduced localization accuracy [40].

A. Related Work

To the best of the author's knowledge, there are no compact, robust and scalable UWB antenna arrays found in literature that are tailored towards IR-UWB applications that require joint distance and 2D AoA estimation. Current multi-antenna UWB localization systems often leverage bulky arrays, constructed based on conventional UWB antennas, such as horn [47], [48] or Vivaldi-like [49]–[51] antennas, and are optimized and evaluated in terms of their system-level time-domain performance [48], [50] or grating lobe suppression [50], [51]. However, they are interconnected by long coaxial cables, leading to complex, bulky and stationary systems, impeding their scalability. Recently, IR-UWB ICs and corresponding multi-antenna PCB evaluation boards have been developed, both commercially [34]–[36], [52] and in scientific publications [37], [53]. These PCBs provide compact integration with planar UWB arrays, but the number of antenna elements is fixed and limited due to side-by-side electronics integration, not only hindering upscaling to larger 2D UWB arrays, but also leading to large system footprints. Furthermore, as indicated in comparison Table V (Section IV-E), these systems often adopt ceramic chip antennas [37], [38], [53], known for their suboptimal antenna performance.

When dissecting the state-of-the-art on UWB antenna design, on the one hand several scalable UWB antenna arrays are encountered [54]–[56]. However, the modular all-metal array presented in [54] exhibits a height larger than $\lambda/2$, while tightly coupled arrays [55], [56] require an intricate feeding

network. Moreover, none are optimized in the time domain or at system level. On the other hand, a plethora of time-domain-optimized planar and cost-effective PCB-based UWB monopole or dipole antennas have been proposed [57]–[59], as well as PCB-based UWB arrays [60], [61]. Yet, these are very sensitive to their integration platform, making them unsuitable for the harsh urban shipping environments. Moreover, their omnidirectional radiation leads to position ambiguity.

Dielectric resonator antennas (DRAs) offer a wide bandwidth in a compact footprint and allow for direct integration of active electronics behind their ground plane, paving the way for compact and scalable arrays [62], [63]. However, none of these arrays have been optimized in the time domain. Moreover, the very few DRA elements that report their time-domain performance [64], [65], suffer from excessive pulse distortion, indicated by a fidelity factor of only 80 %.

Finally, cavity-backed antennas feature high isolation from their integration platform and facilitate integration in arrays with low mutual coupling [66], [67], but typically at the expense of a narrow bandwidth or large footprint [67]. Recently, the air-filled substrate-integrated-waveguide (AFSIW) technology has been established as a key technology to satisfy all these conflicting demands [68]–[70]. It enables the realization of highly efficient IR-UWB cavity-backed slot antennas in low-cost PCB technology that facilitate active electronics integration and exhibit excellent time-domain performance [71]. Yet, their footprint is too large for $\lambda/2$-spaced arrays, prohibiting the realization of 2D multi-antenna nodes as needed for 3D positioning in loading docks and locks. Table IV (Section IV-E) compares these state-of-the-art antenna designs, based on a number of relevant IR-UWB characteristics.

B. Contributions

In this article, we enable joint distance and 2D AoA localization of autonomous vessels in complex urban scenarios with minimal shore-side infrastructure by first proposing a novel IR-UWB antenna element as a building block for cost-effective, high-performance and scalable planar multi-antenna IR-UWB systems. A quarter-mode (QM) AFSIW cavity-backed slot antenna is equipped with a guard trace and a capacitively coupled feed to realize a compact, yet wideband and highly efficient antenna element that maintains its performance when installed on a wide variety of installation platforms, such as a vessel's metal hull and a metal cargo crane. A multi-objective system-level optimization process, based on time-domain figures-of-merit, is adopted to yield a stable radiation pattern over a broad angular and frequency range with minimal pulse distortion, phase fluctuations and range bias. In-depth analysis of different array configurations shows that the modular antenna element maintains performance when embedded in 1D and 2D antenna arrays with a scalable number of antennas owing to its high isolation. Furthermore, the proposed topology is compatible with standard low-cost PCB fabrication techniques and facilitates compact integration with active IR-UWB electronics. To showcase its potential in localization and sensing applications, the antenna is extensively validated in the frequency and time domain.

In a second step, a 2×2 antenna array is manufactured and experimentally validated. A prototype is exploited as multi-antenna node to demonstrate joint distance and 2D AoA estimation in stand-alone conditions and when the array is installed on a metal plate to mimic performance when deployed on a vessel's hull, highlighting the robustness of the array against integration platform effects. This also proves that the proposed antenna is suited for the realization of planar 2D multi-antenna systems, thereby paving the way for 3D positioning in loading docks and locks with minimal shore-side infrastructure.

In a third and final step, three 1×4 antenna array prototypes are each connected to an IR-UWB hardware platform, consisting of four synchronized UWB transceivers, and integrated in a waterproof housing. Next, these UWB positioning nodes are deployed on a vessel to demonstrate performance in complex real-life urban shipping applications. Despite only one shore-side UWB beacon node being deployed, these measurements show that 96 % of AoA errors remain below 10° while guaranteeing a distance estimation error below 10 cm, indicating robust performance in these challenging environments. Note that the proposed antennas are exploited in our previous work [72] and [73], where a UWB positioning node containing the 1×4 antenna array is employed for machine learning-based AoA estimation in noisy and multipath conditions, but neither the topology, nor its multi-objective system-level optimization, nor its performance in urban shipping environments is discussed in those contributions.

The remainder of this article is organized as follows. Section II details the antenna optimization process, describing its specifications, design evolution and multi-objective optimization process. In Section III, the antenna performance, when embedded as an element in arrays of different size, is analyzed through simulations and the manufacturing process is described. Section IV discusses the measurements of the antenna element and the 2×2 array in both the frequency and time domain. An evaluation of the array's distance and 2D AoA estimation performance is also included. Furthermore, the estimation performance of the UWB positioning nodes, incorporating a 1×4 array and deployed on a vessel, is illustrated. Finally, conclusions are drawn in Section V.

II. Quarter-Mode AFSIW Cavity-Backed IR-UWB Antenna

A. Design Requirements for Joint Distance and 2D AoA Estimation

A robust, compact and high-performance antenna that is fully compatible with standard manufacturing techniques, is designed for operation in the [5.9803 GHz; 6.9989 GHz] frequency band, covering UWB channels 5 and 7 of the IEEE 802.15.4z standard [74], [75]. In this band, the return loss, with respect to a 50 Ω impedance, is targeted to exceed 10 dB, which requires a fractional impedance bandwidth (FBW) of at least 15.7 %. For accurate and unambiguous distance and AoA estimation with a planar array, a hemispherical radiation pattern is required, with minimal gain fluctuations as a function of elevation and azimuth angle and over the entire

frequency range. Therefore, a half-power beamwidth (HPBW) of at least 100° and a front-to-back-ratio (FTBR) larger than 10 dB are imposed over the entire targeted frequency band. A high antenna efficiency of at least 90 % is pursued.

When optimizing the system-level and time-domain performance, three figures-of-merit are specified: the relative group delay variation (GDV), the system fidelity factor (SFF) and the distance estimation error (DEE). For the GDV [39], considered over the frequency band $[\omega_0; \omega_n]$, we impose that

$$\mathrm{GDV} = \max_{\omega} \left| \tau_g(\omega) - \frac{1}{\omega_n - \omega_0} \int_{\omega_0}^{\omega_n} \tau_g(\omega) \mathrm{d}\omega \right| \leq 100\,\mathrm{ps}, \tag{1}$$

with $\tau_g(\omega)$ the group delay. For the SFF [76], characterizing the correlation between an input pulse $u(t)$ applied to an antenna link and its corresponding output pulse $v(t)$, considered over the interval $[t_0; t_n]$, we require that

$$\mathrm{SFF} = \max_{t} \left| \frac{\int_{t_0}^{t_n} u(\tau) v(t+\tau) \mathrm{d}\tau}{\sqrt{\int_{t_0}^{t_n} u^2(\tau) \mathrm{d}\tau \int_{t_0}^{t_n} v^2(\tau) \mathrm{d}\tau}} \right| \geq 98\,\%. \tag{2}$$

Finally, we desire for the DEE [42],

$$\mathrm{DEE} = |t_{\max}(\theta, \phi) - t_{\max}(0, 0)| \cdot c \leq 3\,\mathrm{cm}, \tag{3}$$

where c is the speed of light and $t_{\max}(\theta, \phi)$ is the orientation-dependent time-of-arrival of a UWB pulse that maximizes the SFF in a certain direction (θ, ϕ). These criteria are enforced in both UWB channels 5 and 7 and in the HPBW of the antenna. Moreover, all aforementioned figures-of-merit should exhibit excellent immunity to platform effects.

Finally, to guarantee compatibility with state-of-the-art PDoA-based AoA estimation algorithms, when seamlessly incorporating the antenna in both 1D and 2D array configurations, a maximum inter-element distance of $\lambda/2$ is imposed [35]. For correct operation in the entire targeted frequency range, this free-space wavelength $\lambda = \lambda_{\min}$ should correspond to the highest frequency of operation $\mathrm{f_{max}}$, being 6.9989 GHz. Therefore, to support state-of-the-art 2D AoA estimation algorithms, the antenna must fit in a 21.4 mm × 21.4 mm footprint and the mutual coupling between any two antenna elements should remain below −15 dB.

B. Compact, Robust and Wideband Antenna Element

To meet this extensive set of stringent design requirements, a novel antenna topology is proposed: a capacitively-coupled-fed guard-trace-based QM-AFSIW cavity-backed slot antenna. Fig. 1 illustrates how a large and narrowband AFSIW cavity can be transformed into this innovative topology that enables scalable IR-UWB antenna arrays supporting joint distance and 2D AoA estimation. The topology consists of a radiating L-shaped slot and a QM-AFSIW cavity with guard trace, implemented through metal edge-plating in a low-cost PCB. The antenna is fed by a coaxial probe, of which the outer conductor is connected to the cavity's bottom conductive layer. Its inner conductor is connected to a metal annular ring on top of the cavity to capacitively couple with the top conductive

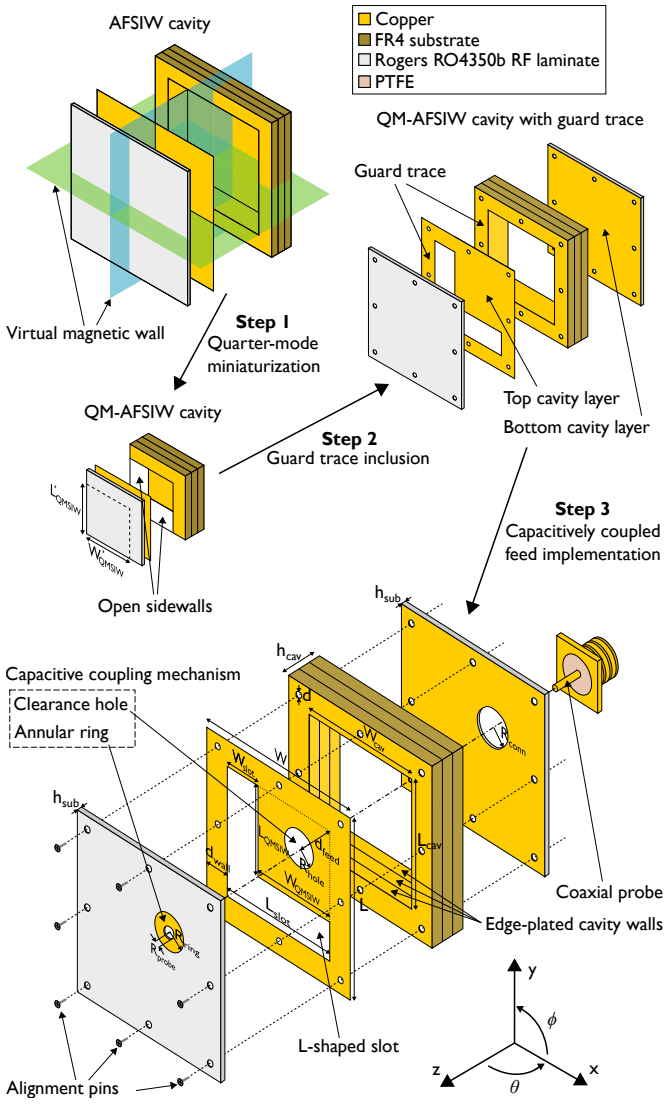

Fig. 1: Schematic overview of the proposed antenna topology and its design evolution, with annotated design parameters.

layer of the cavity, in which a clearance hole is created. The flowchart in Fig. 2 depicts the optimization strategy, linking all optimization steps to the design steps in Fig. 1. It focuses on the optimization goal introduced in each step and includes all relevant design parameters. Note that each goal remains valid in the subsequent optimization steps.

As depicted in Fig. 1, an AFSIW cavity, designed such that its $\mathrm{TE_{110}}$-mode resonates at a center frequency of $\mathrm{f_c}$ = 6.4896 GHz, corresponding to the center frequency of UWB channels 5 and 7, serves as the fundamental building block for the proposed design. By applying the quarter-mode miniaturization technique [77] in Step 1, a QM-AFSIW cavity is obtained with a footprint of only $\mathrm{L'_{QMSIW}} \times \mathrm{W'_{QMSIW}}$ = 16.3 mm × 16.3 mm. While the cavity's footprint is reduced by a factor 4, radiation through its open sidewalls decreases its ability to shield electromagnetic fields, making the antenna performance vulnerable to integration platform effects and the topology unsuitable for incorporation in compact arrays.

To improve the cavity's self-shielding and to allow radiation

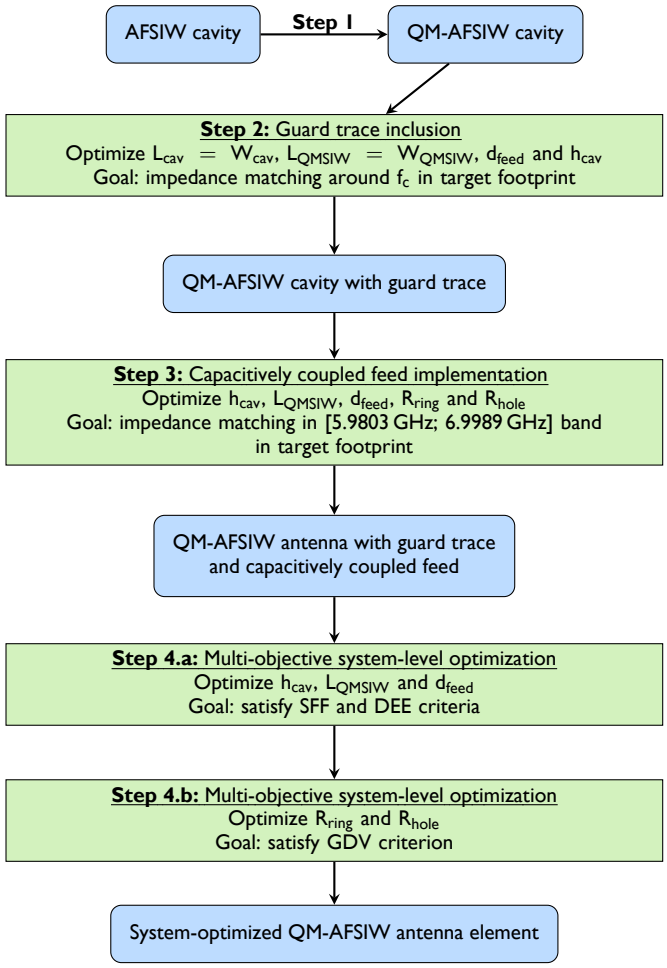

Fig. 2: Flowchart summarizing the optimization strategy.

through the antenna cavity's top plane, a guard trace along the open sidewalls is included in the second design step (Fig. 1). While this seems to cause a significant size increase [77], the capacitive loading effect of the guard trace on the cavity enables a reduction of the antenna size to below the targeted footprint. Based on full-wave simulations in CST Microwave Studio's frequency-domain solver, (Step 2, Fig. 2), the optimal guard trace position is determined, yielding a final antenna footprint of only $L_{cav} \times W_{cav} = 19\,\text{mm} \times 19\,\text{mm}$ ($0.44\,\lambda_{min} \times 0.44\,\lambda_{min}$), including the radiating slot. By including the guard trace, the original QM-AFSIW cavity footprint $L'_{QMSIW} \times W'_{QMSIW}$ has been reduced by a factor 1.73, yielding $L_{QMSIW} \times W_{QMSIW} = 12.4\,\text{mm} \times 12.4\,\text{mm}$. Because of the shielding capabilities of the resulting QM-AFSIW cavity with guard trace, low mutual coupling can be guaranteed when embedding the element in a compact array and undesired back radiation is minimized, resulting in a high FTBR.

To excite the TE_{110}-mode in the QM-AFSIW-based topology with minimal back radiation, a coaxial feed is adopted. To ensure broadband impedance matching within the compact footprint, the height of the antenna cavity h_{cav} can be increased to lower its Q-factor. Yet, for larger cavity heights, an increased coaxial probe feed length is accompanied by a larger feed inductance, making proper impedance matching difficult. This effect can be observed in Fig. 3, depicting the achievable FBW of the antenna element as a function of the cavity height h_{cav}. The achievable bandwidth is the maximal bandwidth that can be reached without considering any other optimization criterion. It is obtained by tuning the coaxial probe position d_{feed} and the $L_{QMSIW} = W_{QMSIW}$ dimension, while the antenna footprint remains fixed at $L_{cav} \times W_{cav} = 19\,\text{mm} \times 19\,\text{mm}$. The blue curve shows that the bandwidth improvement indeed saturates for larger cavity heights and that the targeted FBW of 15.7 % cannot be reached.

To counteract the feed probe's inductance and enhance the impedance bandwidth, the feeding mechanism is adapted to capacitively couple the feed probe to the antenna cavity [78]. This corresponds to the third design step in Figs. 1 and 2. In particular, a clearance hole is created in the top metal layer of the antenna cavity. Instead of directly connecting the inner conductor of the coaxial probe to this layer, it is connected to an annular ring, located at a distance of $h_{sub} = 0.25\,\text{mm}$ above this layer and aligned with the clearance hole. The capacitive coupling between the annular ring and the top cavity layer compensates for the additional inductance introduced by the longer coaxial probe. By adjusting the annular ring radius R_{ring} and clearance hole radius R_{hole}, the magnitude of the antenna's input impedance is modified to ensure broadband impedance matching.

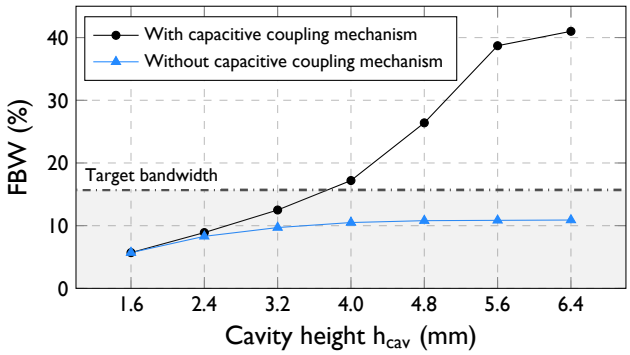

Fig. 3: Fractional impedance bandwidth (FBW) vs. cavity height h_{cav} with and without the capacitive coupling mechanism.

To prove the effectiveness of the capacitively coupled feed, Fig. 3 also shows the achievable FBW of the antenna for different cavity heights when the coupling mechanism is implemented. The depicted results are obtained by judiciously tuning the R_{ring} and R_{hole} parameters as well as the d_{feed} and L_{QMSIW} dimensions. The antenna footprint dimensions remain fixed. It can be observed that the bandwidth is now significantly enlarged by increasing h_{cav}. With the mechanism implemented, the achievable FBW can easily exceed 30 %. Note that a cavity height of $h_{cav} \geq 4.0\,\text{mm}$ is necessary to achieve broadband matching over the targeted [5.9803 GHz; 6.9989 GHz] frequency band. In this third optimization step (Fig. 2), suitable values for h_{cav} and the associated parameter values for L_{QMSIW}, d_{feed}, R_{ring} and R_{hole} are determined through full-wave simulations. The symmetry of the proposed topology with respect to the $\phi = 45°$-plane leads to a linearly polarized antenna with its co-polarization and cross-polarization axis along the $\phi = 45°$- and $\phi = 135°$-plane, respectively.

This article has been accepted for publication in IEEE Sensors Journal. This is the author's version which has not been fully edited and
content may change prior to final publication. Citation information: DOI 10.1109/JSEN.2023.3310992

C. System-Oriented and Time-Domain-Based Design Approach

Guaranteeing excellent localization accuracy requires outstanding antenna performance in both the frequency and time domain, and at the system level. Therefore, a dedicated in-house optimization framework [71] is exploited to evaluate the system-level time-domain figures-of-merit put forward in Section II-A. The framework simulates a free-space antenna link, consisting of the proposed antenna element at both transmit and receive sides, with a distance of 1 m separating both antennas. It evaluates the SFF, the GDV and the DEE for different angles of departure and arrival in the positive hemisphere ($z > 0$, Fig. 1) of the transmit and receive antenna, respectively. To do this, it relies on full-wave simulations of the individual antennas and applies an upconverted root raised cosine (RRC) pulse to the antenna link to assess the introduced pulse distortion. Specifically, the reference RRC pulses $r(t)$ for UWB transmitters in UWB channels 5 and 7 are applied, as defined in [74]. These normalized pulse amplitudes modulate a carrier sine wave, $(1 + r(t))\sin(2\pi f_c t)$, after which their amplitude is normalized again.

First, the framework is applied to analyze the time-domain performance of the antenna element. Therefore, the SFF and GDV of the bandwidth-optimized designs, whose FBW is shown in Fig. 3, are determined. The results are depicted in Fig. 4a, showing the worst-case SFF and GDV in the HPBW of the antenna. It can be observed that the SFF and GDV criteria are not met after merely optimizing the antenna to cover the targeted frequency band in the desired footprint. This can be attributed to angular and frequency-dependent variations in both magnitude and phase of the radiation pattern, for which the antenna element has not yet been optimized. Hence, an additional multi-objective optimization step in both the frequency and time domain is required. Therefore, an extensive parameter study is executed to determine which design parameters influence antenna performance with respect to the considered figures-of-merit. Based on these results, a two-step multi-objective antenna optimization process (Step 4, Fig. 2) is performed using the in-house optimization framework to improve the antenna's system-level performance while retaining broadband matching, compact footprint, high efficiency and self-shielding. First, in substep 4.a, the optimal values for h_{cav}, L_{QMSIW} and d_{feed} are determined, focusing on the SFF and DEE criteria. Next, in substep 4.b, the R_{hole} and R_{ring} parameters are modified to satisfy the GDV requirement. The trade-offs that were considered during this optimization process are illustrated in Fig. 4, depicting the antenna's worst-case SFF and GDV within its HPBW.

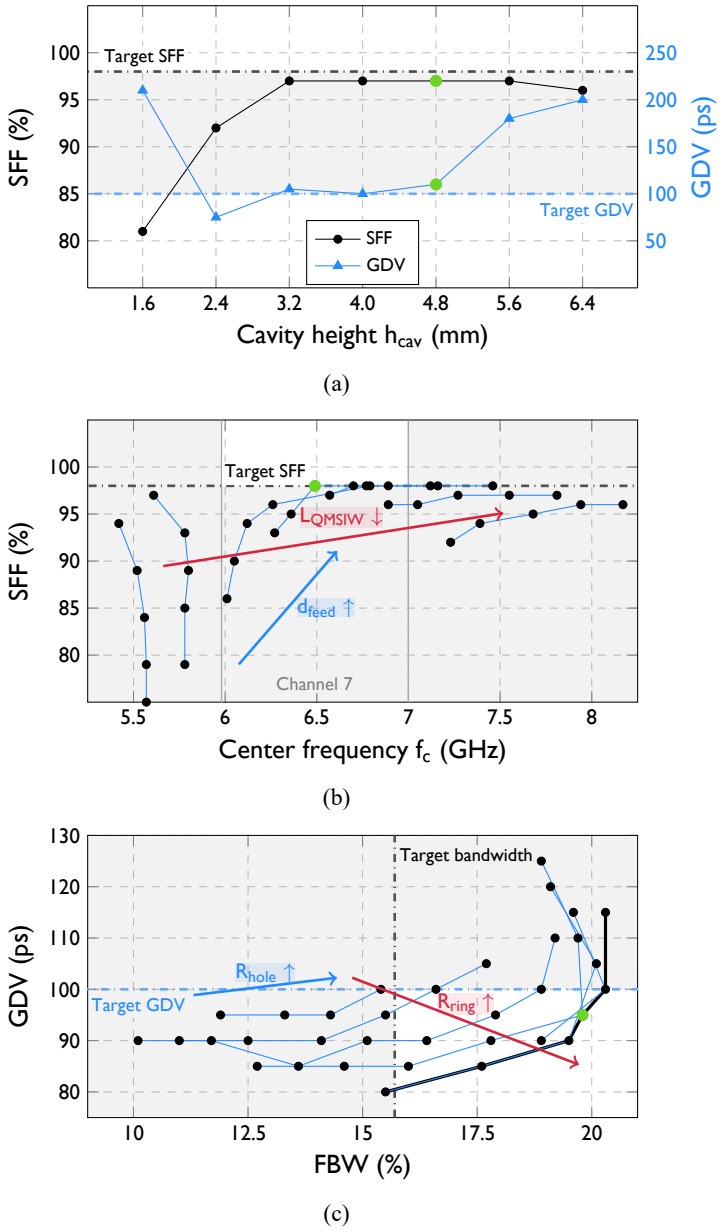

Fig. 4: Multi-objective antenna optimization process: (a) system fidelity factor (SFF) and relative group delay variation (GDV) of bandwidth-optimized designs for different cavity heights (b) SFF vs. center frequency f_c trade-off with selected optimization result (green dot) (c) Pareto-curve (full black line) and Pareto-optimal solution (green dot) illustrating the GDV vs. FBW trade-off by tuning the capacitive coupling mechanism. All curves show worst-case values over the antenna's half-power beamwidth.

Substep 4.a of the multi-objective optimization strategy considers h_{cav}, L_{QMSIW} and d_{feed} (Fig. 2). The results in Fig. 3 and Fig. 4a show that, while $h_{cav} \geq 4.0$ mm is necessary to achieve the targeted bandwidth, larger cavity heights ($h_{cav} \geq 5.6$ mm) lead to quickly deteriorating time-domain performance. Additionally, the parameter study shows that enlarging W_{slot} (decreasing L_{QMSIW}) or d_{feed} can considerably increase the SFF. However, in the compact antenna footprint (fixed to $L_{cav} \times W_{cav} = 19$ mm $\times$ 19 mm), this inevitably leads to an upward shift of the operating frequency band. This is illustrated in Fig. 4b. It shows a set of f_c-SFF pairs, obtained by sweeping the L_{QMSIW} and d_{feed} parameters simultaneously, while keeping the antenna footprint and slot length L_{slot} constant. Increasing d_{feed} generally increases the SFF. However, the L_{QMSIW} dimension is also crucial to satisfy the SFF criterion: while for larger L_{QMSIW}-values this criterion cannot be met, smaller values cause the operating frequency to shift upwards and outside of the targeted frequency band. By

simultaneously considering h_{cav}, L_{QMSIW} and d_{feed} in substep 4.a and optimizing for high SFF and low DEE over the targeted HPBW, a stable radiation pattern is obtained over the operating frequency band, leading to a highly efficient antenna element with a nearly frequency-independent hemispherical radiation pattern with large HPBW and FTBR in the required footprint. This optimization step results in final values of $L_{QMSIW} = 12.4\,\text{mm}$, $d_{feed} = 8.9\,\text{mm}$ and $h_{cav} = 4.8\,\text{mm}$. The corresponding optimization results are indicated in Figs. 4a and 4b (green dot).

In substep 4.b (Fig. 2), the capacitive coupling mechanism is optimized further to tune the phase of the antenna's input impedance to minimize the GDV of the antenna. Hence, the capacitive coupling mechanism, controlled by R_{hole} and R_{ring}, is not only exploited to enhance the antenna bandwidth, but also to minimize its GDV. The ensuing trade-off between meeting the GDV constraint and covering the targeted frequency band is illustrated in Fig. 4c. It shows several FBW-GDV pairs, generated by simultaneously sweeping the R_{ring} and R_{hole} parameters, while keeping the cavity size, slot length and previously optimized h_{cav}, L_{QMSIW} and d_{feed} parameters constant. In general terms, increasing R_{hole} increases both bandwidth and GDV. Increasing R_{ring} enhances the bandwidth, while simultaneously reducing the GDV, provided that R_{hole} is properly adjusted to prevent the GDV from sharply increasing. The resulting Pareto-front is also depicted in Fig. 4c, together with the Pareto-optimal solution. Selecting this solution results in the final antenna dimensions, yielding high bandwidth and large HPBW while satisfying the requirements for the system-level time-domain characteristics. The final dimensions for the optimized antenna element are shown in Table I.

TABLE I:
FINAL VALUES OF THE ANTENNA DESIGN PARAMETERS.

Parameter	Dimension (mm)	Parameter	Dimension (mm)
L	25	R_{probe}	0.65
W	25	R_{ring}	1.5
L_{cav}	19	R_{hole}	2.1
W_{cav}	19	R_{conn}	2.2
L_{slot}	19	h_{cav}	4.8
W_{slot}	6.6	h_{sub}	0.25
L_{QMSIW}	12.4	d_{feed}	8.9
W_{QMSIW}	12.4	d_{wall}	3
		d	1

III. ANTENNA ARRAYS FOR JOINT DISTANCE AND AOA LOCALIZATION

A. Planar, Scalable IR-UWB Antenna Array

To arrive at highly precise IR-UWB localization systems, suitable for the adoption in harsh urban shipping environments requiring 3D positioning, such as loading docks and locks, a planar and 2D scalable IR-UWB antenna array is highly desired. It has been proven that a larger number of antenna elements can significantly increase AoA estimation accuracy [32], [33]. Furthermore, additional array elements allow for extra redundancy in challenging localization environments, making the distance and AoA estimation more robust against element-level measurement errors, such as missing measurements or significant outliers.

However, embedding an antenna element into an array configuration typically affects its performance [79]. Hence, it is advantageous if the antenna element is modular and does not require reoptimization when it is integrated into arrays. Therefore, the performance of the proposed antenna is analyzed through additional simulations while it is embedded in a 2×2 and 3×3 antenna array. The inter-element distance is fixed to 21.4 mm. This allows for PDoA-based AoA estimation, while the 2.4 mm spacing between adjacent antenna cavities provides sufficient mechanical stability during the fabrication and assembly process.

Table II compares the relevant simulated frequency- and time-domain figures-of-merit for the antenna element in stand-alone conditions and when embedded in either a 2×2 or a 3×3 array. Note that it lists the worst performing array element for every frequency-domain figure-of-merit. It can be observed that the impedance bandwidth of the antenna element remains approximately the same. The FBW of all array elements lies between 21.1 % and 24.1 % and every element remains matched in at least the 5.83 GHz – 7.07 GHz range. Hence, the proposed antenna element covers the targeted frequency band when embedded in either array. The mutual coupling between any two elements in the 2×2 array remains below −16.3 dB. For the 3×3 array, the coupling between the inner element and its neighboring elements at its slot sides is slightly higher, but still remains below −14.5 dB.

The element's stand-alone radiation pattern exhibits a peak gain of 4.7 dBi, with a HPBW ranging from −50° to 55°, slightly exceeding the targeted value of 100°. The embedded radiation patterns of the antenna element, obtained by exciting it while terminating the other array elements by a 50 Ω impedance, are expected to be slightly deformed with respect to the stand-alone pattern, due to mutual coupling and the larger ground plane size of the arrays. Specifically considering the 3×3 array, simulations show that the inner element is the

TABLE II:
PERFORMANCE COMPARISON OF A STAND-ALONE ANTENNA ELEMENT AND AN ANTENNA ELEMENT EMBEDDED IN A 2×2 AND 3×3 ARRAY. (WORST-CASE VALUES OVER THE ANTENNA'S HPBW, AVERAGE μ AND STANDARD DEVIATION σ OVER ALL ELEMENTS.)

Figure-of-merit	Single element	Array	
		2×2	3×3
FBW (%)	19.7	21.1	22.1
Mut. coup. (6.5 GHz) (dB)	-	-16.3	-14.5
Peak gain (6.5 GHz) (dBi)	4.7	4.9	4.3
Channel 7		μ (σ)	
SFF (%)	98.1	98.3 (0.3)	98.1 (0.4)
GDV (ps)	95	94 (6)	93 (20)
DEE (mm)	4	12 (3)	15 (6)
Channel 5		μ (σ)	
SFF (%)	99.5	99.5 (0.1)	99.4 (0.1)
GDV (ps)	40	36 (3)	43 (17)
DEE (mm)	5	12 (3)	15 (6)

most directive, with a peak gain of 5.0 dBi, a HPBW of 90° and a FTBR of 13 dB. One of the edge elements yields the smallest peak gain of 4.3 dBi. In conclusion, the embedded antenna element exhibits a wide HPBW and large FTBR, with a peak gain that remains quasi constant, even when embedded in an array configuration.

The small variations in the embedded radiation patterns, with respect to that of the stand-alone antenna element, inevitably lead to small deviations for the imposed time-domain figures-of-merit. To analyze the antenna performance in this regard, Fig. 5 compares the angle-dependent time-domain simulation results for UWB channel 7 of the inner and an outer element of the 3×3 array with the stand-alone element. Note that for the 2×2 array, every element can be considered an outer element. Within the antenna's HPBW, considered to range from −50° to 50°, the SFF remains above 98 % in all considered scenarios. Moreover, the GDV remains below 100 ps and the DEE below 30 mm.

Table II provides a more complete overview by listing the time-domain figures-of-merit for the stand-alone antenna element and the 2×2 and 3×3 array elements. In particular, it reports the worst-case values over the antenna's HPBW for UWB channels 5 and 7. For the array elements, the average μ and standard deviation σ of these worst-case values are reported, considered over all elements in the respective array. The results show that all imposed design requirements in both channels are met. The largest standard deviation is observed for the GDV of the 3×3 array. In this array, the two corner elements on the main array diagonal exhibit a GDV that deviates from the mean, but it does stay below 85 ps for UWB channel 5. The slight increase in GDV can be attributed to diffraction along both array edges. In conclusion, based on the simulation results, the proposed antenna element retains its performance when embedded in array configurations. Owing to its inherent self-shielding, it can be readily incorporated without reoptimization in scalable 1D and 2D arrays supporting joint distance and AoA estimation.

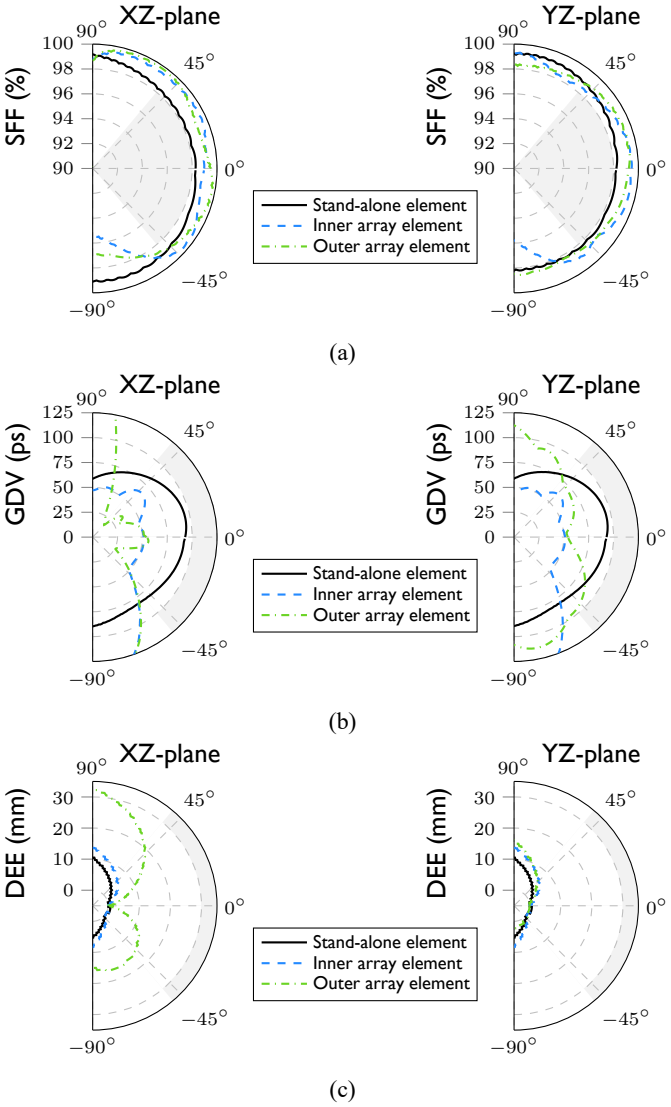

Fig. 5: Simulated time-domain performance (UWB channel 7) of a stand-alone antenna element and an inner and outer embedded element in a 3×3 array: (a) SFF, (b) GDV and (c) DEE.

B. Manufacturing Process of the Realized Prototypes

Multiple prototypes of the single antenna element, a 2×2 array and a 1×4 array have been realized. A 2×2 array topology is selected to showcase 2D AoA estimation, while keeping all measurements in Section IV manageable. A 1×4 array is selected for the adoption in the UWB positioning nodes that are deployed on a vessel. A major advantage of the AFSIW technology is its straightforward realization in widely-available PCB technology [69]–[71]. This allows for a cost-effective manufacturing process using common PCB manufacturing techniques and low-cost materials. The top and bottom views of a realized antenna prototype, as well as the corresponding PCB layer stack-up, are shown in Fig. 6a. A picture of a realized 2×2 and 1×4 array prototype is depicted in Fig. 6b and Fig. 6c, respectively.

Three 1.55 mm-thick FR-4 substrates are used to implement the metallic sidewalls of the antenna cavity. Therefore, a square cavity is milled out in these PCB layers, which are then gold-plated on all sides by round-edge plating. A 0.25 mm-thick two-layer Rogers RO4350b laminate ($\epsilon_r = 3.66$ and $\tan\delta = 0.0037$) is applied as top and bottom substrate. The bottom metal layer of the top Rogers high-frequency laminate implements the top metal layer of the cavity, containing the L-shaped slot and a clearance hole for the inner conductor of the feed probe. Its top metal layer realizes the annular ring, implementing the capacitive coupling. The top metal layer of the bottom Rogers high-frequency laminate implements the bottom metal layer of the cavity. Its bottom metal layer contains a solder platform that is connected to its top layer by via rows. This solder platform facilitates the assembly of the coaxial feed, for which a straight SMA square flange mount coaxial connector by Multicomp is used. The outer conductor of the coaxial feed is soldered to the solder platform and its inner conductor to the annular ring on the top Rogers laminate. In future work, the bottom Rogers RO4350b laminate can be reused to compactly integrate active components, such as a UWB transceiver and microcontroller, reducing intercon-

nection losses and system footprint to the bare minimum, thereby paving the way for compact and high-performance active multi-antenna UWB positioning nodes.

For mechanical stability, the outside edges of the realized prototypes are 3 mm wide. The 2.4 mm spacing between the cavity walls of adjacent antenna elements in the array prototype, made possible by the compactness of the individual antenna element, provides mechanical stability in between the cavities. This also leads to a large electrical contact area between the stacked PCB layers. To guarantee sufficient electrical contact and correct alignment of the different PCB layers composing the antenna, brass M1 screws are used. They are placed along the edges of the prototypes and in between the elements, such that every cavity is surrounded by screws as depicted in Fig 6. Full-wave simulations indicate negligible influence of the screws on the antenna's performance. Taking the outside edges of the prototypes into account, the total dimensions of a single-element prototype equal 25 mm × 25 mm × 5.15 mm, while the 2×2 and 1×4 array prototype's dimensions equal 46.4 mm × 46.4 mm × 5.15 mm and 89.2 mm × 25 mm × 5.15 mm, respectively.

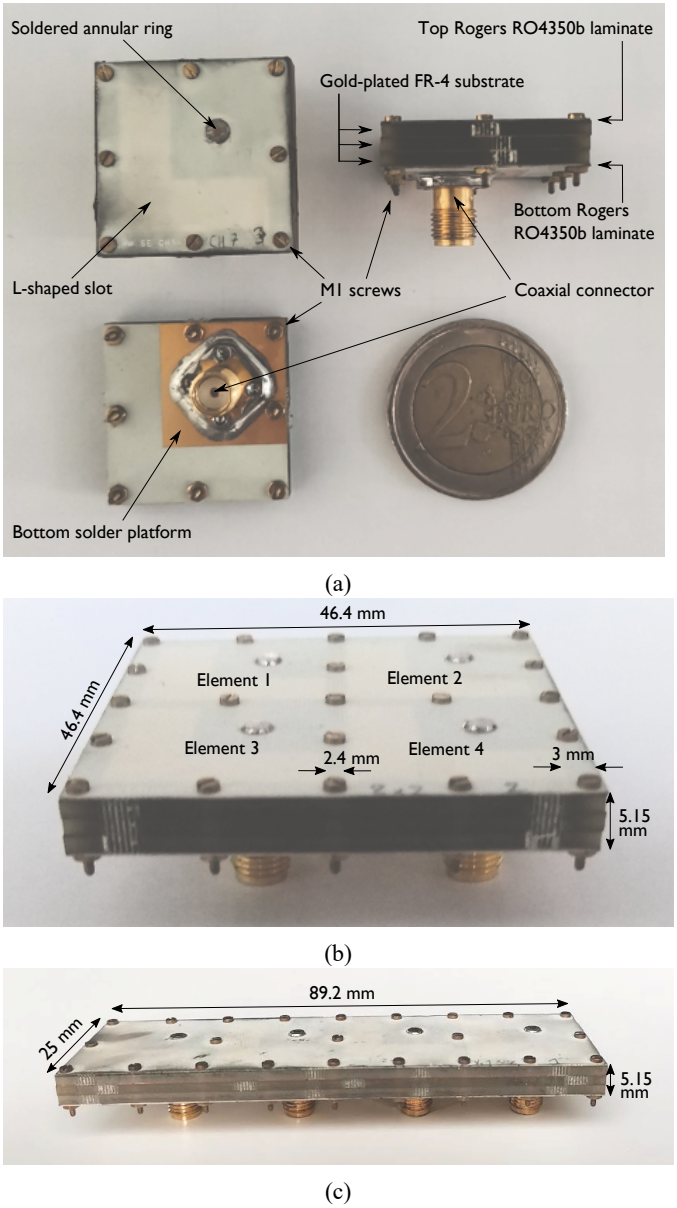

Fig. 6: Manufactured prototypes: (a) antenna element, (b) 2×2 array and (c) 1×4 array.

IV. Experimental Validation

A. Performance of the Single Antenna Element

First, the frequency-domain performance of the stand-alone single antenna element is verified in an anechoic chamber, using a Keysight N5242a PNA-X network analyzer and an NSI-MI spherical near-field scanner. Then, its performance is evaluated in worst-case deployment scenarios by deploying it directly on a 35 cm × 35 cm copper plate. The metal plate simulates a vessel's metal hull, generating severe integration platform effects. Fig. 7 depicts the measured reflection coefficient of two prototypes, in stand-alone conditions, together with the free-space stand-alone simulations. Note that the measured bandwidth is slightly smaller than expected from simulations. This can be attributed to small deviations in the manufacturing and assembly process. Nevertheless, both prototypes cover the targeted frequency band, resulting in an FBW of 17.6 %, compared to 19.7 % in simulations. Moreover, both realized prototypes show little deviation with respect to each other, indicating good manufacturing reproducibility. Fig. 7 also shows that the antenna's reflection coefficient and bandwidth remain almost invariable when the antenna is mounted on a

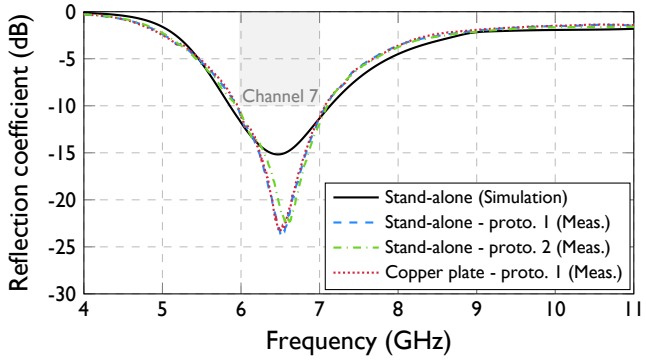

Fig. 7: Measured and simulated reflection coefficient of the single-element prototypes in different deployment scenarios.

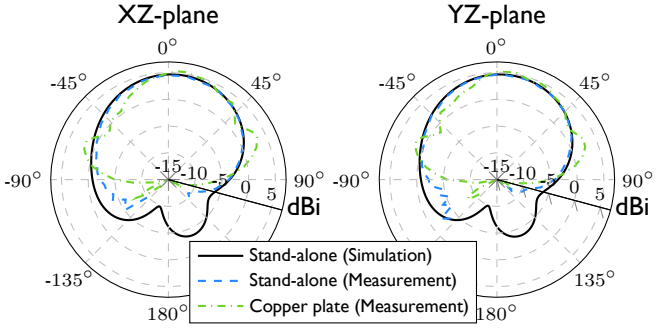

Fig. 8: Measured and simulated radiation pattern of the single-element prototype, at 6.5 GHz, with and without copper plate.

copper plate. This indicates robust and platform-independent performance, validating the self-shielding characteristics of the proposed antenna topology.

Fig. 8 depicts the measured radiation patterns of the antenna at 6.5 GHz in stand-alone conditions and when deployed on a copper plate. The radiation patterns are measured in both the XZ- and YZ-plane, as defined in Fig. 1. A very good agreement between measurements and simulations in stand-alone conditions is obtained. When the antenna is deployed on a copper plate, the radiation pattern becomes slightly more directive and exhibits small sidelobes, which are directly caused by diffraction at the copper plate edges. However, although some deformation is present in the radiation pattern, it is still very similar to the stand-alone pattern. The measured peak gain equals 5.5 dBi, compared to 4.8 dBi in stand-alone conditions. Radiation pattern measurements have also been executed at 6 GHz and 7 GHz. Table III (top) lists the obtained results at these frequencies and at 6.5 GHz, comparing them to the corresponding simulated values. The selected frequencies represent the start, center and stop frequency of the targeted UWB channel 7 frequency band, respectively. The results show little deviation between the measurements and simulations or when considering different frequencies. A measured peak gain higher than 4.5 dBi, with a HPBW of 100° and an efficiency > 91 %, is obtained over the entire frequency band. The radiation patterns at 6 GHz and 7 GHz are also evaluated when the antenna is deployed on a copper plate. Similar to the observations in stand-alone conditions, the radiation pattern remains stable over the entire targeted frequency range, indicating good performance with respect to integration platform effects in the harsh deployment scenarios encountered on vessels in urban shipping applications. Similar results are also obtained at 6.25 GHz and 6.75 GHz, the start and stop frequencies of the UWB channel 5 frequency band.

System-level measurements have been conducted to validate the antenna element's time-domain performance. An antenna link, set up between both developed prototypes, is characterized in an anechoic chamber. By measuring the appropriate S-parameters, using the Keysight N5242a PNA-X network analyzer, the transfer function of this link is determined.

TABLE III:
FREQUENCY- AND TIME-DOMAIN CHARACTERISTICS OF THE SINGLE-ELEMENT PROTOTYPE IN FREE-SPACE STAND-ALONE CONDITIONS.

Frequency	6.0 GHz		6.5 GHz		7.0 GHz	
	Sim.	Meas.	Sim.	Meas.	Sim.	Meas.
Peak gain (dBi)	4.7	5.0	4.7	4.8	4.3	4.5
FTBR (dB)	11.1	-	10.9	-	10.5	-
Total eff. (%)	94	92	97	98	93	91
HPBW XZ (°)	105	100	105	100	105	100
HPBW YZ (°)	105	100	105	100	105	100

UWB channel	Channel 5		Channel 7	
	Sim.	Meas.	Sim.	Meas.
SFF (%)	99.5	99.7	98.1	98.8
GDV (ps)	40	54	95	93
DEE (mm)	5	14	4	13

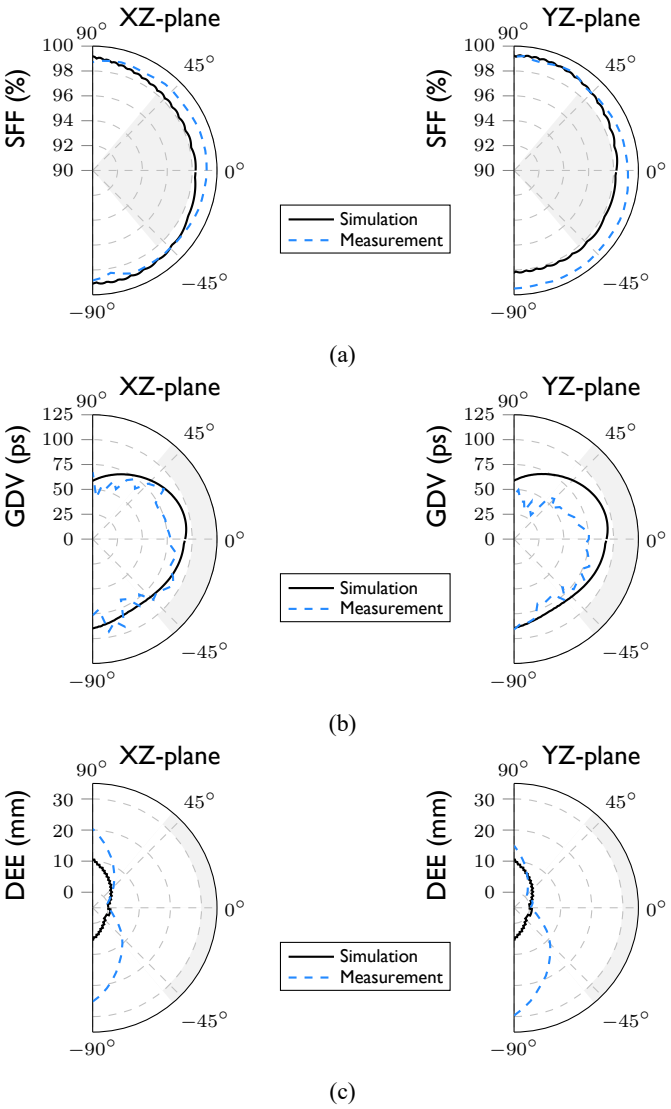

Fig. 9: Time-domain performance (measurements and simulations) of the single antenna: (a) SFF, (b) GDV and (c) DEE.

Subsequently, the GDV, SFF and DEE are obtained according to (1) – (3). Similar to the simulations performed in the optimization framework, the upconverted RRC pulse specified in Section II-C is applied to determine the SFF and DEE. The angle-dependent results for UWB channel 7 are depicted in Fig. 9. Table III (bottom) summarizes the measurement results for UWB channels 5 and 7 and compares them to the simulated values. Note that the worst-case values within the antenna's HPBW are listed. A good agreement between measurements and simulations is obtained and the targeted specifications are met in the HPBW of the antenna. Hence, the proposed antenna shows solid phase stability and minimal pulse distortion and ranging estimation bias, making it suitable for IR-UWB applications.

B. Frequency-Domain Performance of the 2×2 Array

The 2×2 array prototype is also validated in an anechoic chamber in stand-alone conditions. Fig. 10 shows the measured reflection coefficient of the four antenna elements,

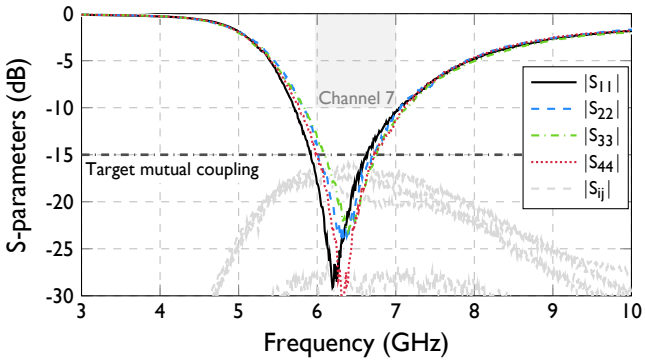

Fig. 10: Measured S-parameters of the 2×2 antenna array.

demonstrating proper matching over the entire targeted frequency band. The FBW of the four elements lies between 19.4 % and 21.0 %, compared to 21.1 % and 23.2 % in simulations. The measured mutual coupling between any two elements is also shown in Fig. 10. It does not exceed −16 dB, highlighting that the proposed antenna element provides low mutual coupling when embedded in an array, paving the way for straightforward integration in high-performance, scalable 2D arrays and compact practical systems. Fig. 11 shows the measured and simulated radiation patterns of the 2×2 array's elements at 6.5 GHz. Again, there is excellent agreement between measurements and simulations. The measured peak gain of the elements ranges between 5.0 dBi and 6.0 dBi, compared to 4.9 dBi and 5.4 dBi in simulations.

C. Joint Distance and 2D AoA Estimation Performance in a Lab-Based Scenario

To validate the joint distance and AoA estimation performance of the 2×2 array, a dedicated measurement setup is devised, as shown in Fig. 12. An antenna link is established consisting of a single-element prototype and an array prototype, operating as the tag and anchor antenna, respectively. The tag antenna is attached to a robot arm that provides controlled and submillimeter-level accurate movement in a plane parallel to the YZ-plane, as defined in Fig. 12. The anchor is installed on a 3D-printed mount, which also fixates the RF cables to ensure minimal cable displacement. To determine the position of the tag, based on distance and 2D AoA estimation, the four channels between the single-element tag and the four-element anchor are measured using the Keysight N5242a PNA-X network analyzer. Because this network analyzer is limited to 4-port measurements, an RF switch [80] is used to select the appropriate anchor element. The measurement setup is fully automated and care is taken to perform separate calibration steps for every state of the RF switch, which are automatically reloaded every time a different anchor element is selected.

Measurements are conducted to evaluate the distance and AoA estimation accuracy of the anchor array in stand-alone conditions and when it is directly deployed on a copper plate, to mimic the integration platform effects introduced by the hull of a vessel. The tag is placed at a distance of $\Delta x = 40$ cm from the anchor and moved along a grid of 16×11

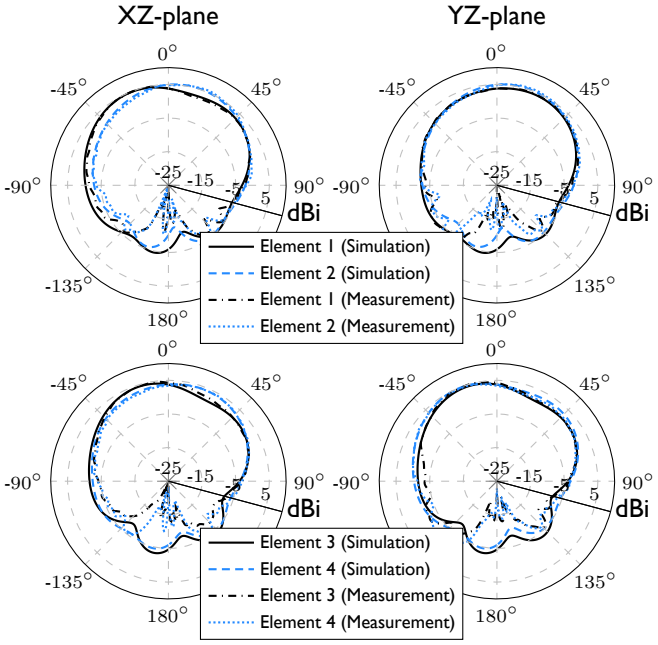

Fig. 11: Measured and simulated radiation patterns of the 2×2 antenna array.

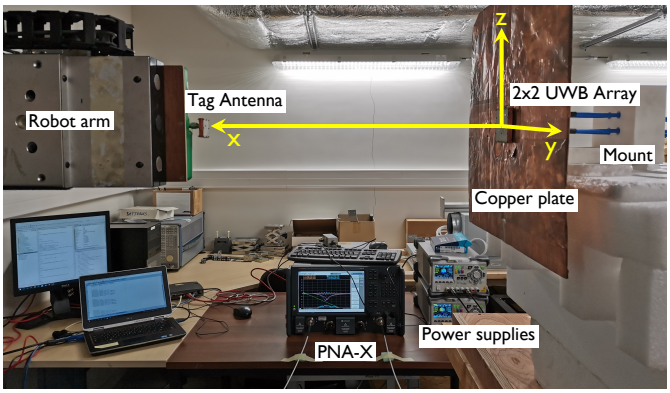

Fig. 12: Dedicated measurement setup for joint distance and 2D angle-of-arrival (AoA) estimation validation.

positions, resulting in 176 measurement points. A fixed step of 2 cm is adopted between grid points for which the azimuth or elevation angle remains below 45°. For larger angles, the grid step is increased to 4 cm. This fixed grid is shown in Fig. 13, according to the coordinate system defined in Fig. 12. By moving the tag along this grid, the distance d_{ta} between tag and anchor, and the azimuth ϕ and elevation θ angles-of-arrival of the signal received at the anchor are varied, according to

$$d_{ta} = \sqrt{x^2 + y^2 + z^2} \tag{4}$$

$$\phi = \arctan\left(\frac{y}{x}\right) \tag{5}$$

$$\theta = \arctan\left(\frac{z}{\sqrt{x^2 + y^2}}\right) \tag{6}$$

In this way, distances ranging from 40 cm to 100 cm, azimuth angles from 0° to 63° and elevation angles from 0° to 45° are considered. Note that θ is defined such that the azimuth plane

(XY-plane) corresponds to $\theta = 0°$.

Based on the measured transfer functions, both a distance estimate and a 2D AoA estimate are computed. Since the purpose of this article is to highlight the joint distance and 2D AoA estimation capabilities of the antenna array and not the positioning algorithm, we demonstrate the array's potential to provide accurate estimates for both quantities separately. The distance is estimated by using a ToA approach for each of the four tag-anchor channels, using the upconverted RRC pulse as described in Section II-C. The final distance estimate is calculated by averaging the four initial estimates. 2D AoA estimation is performed by applying the MUSIC algorithm [73], [81]. A post-processing calibration step is applied to the resulting distance and 2D AoA estimates to account for initial misalignment by comparing nine of the measurement points to their ground truth values.

The estimation results are depicted in Fig. 13, on top of the grid, parallel to the YZ-plane, along which the tag is moved (ground truth). For several points on this grid, the estimated grid points are shown and explicitly compared to the ground truth points. Note that not all estimates are shown to not overload the figure. The estimated grid points are computed based on the estimated distance d_{ta} and azimuth ϕ and elevation θ angles-of-arrival, using (4) – (6). A very good agreement is obtained between all estimated grid positions and their ground truth, both with an anchor in stand-alone conditions and deployed on a copper plate.

A more detailed overview of the estimation errors of the separate distance and angle estimates is depicted in Fig. 14. Fig. 14a shows the cumulative distribution function (CDF) of the distance errors for all 176 estimates. Fig. 14b and Fig. 14c show the CDFs of the corresponding estimation errors for the azimuth and elevation angle, respectively, covering a field-of-view of [0°, 63°] in the azimuth plane and [0°, 45°] in the elevation plane. It can be observed that 97 % of the distance errors remain below 1 cm in magnitude when measuring in stand-alone conditions. Moreover, no angular estimation error exceeds 5° in magnitude. Fig. 14 also shows the estimation errors obtained when the anchor is mounted on the copper plate. Two cases are considered. In the first experiment, the measurements with the anchor mounted on the copper plate are recalibrated for this deployment scenario. Now, 95 % of distance errors remain below 1 cm in magnitude and 97 % of angle estimation errors remain below 5° in magnitude. In the second experiment, the post-processing calibration and error coefficients for stand-alone conditions are applied to the measurements involving the copper plate. A slight increase in estimation errors is to be expected, yet all distance errors remain below 2 cm in magnitude, and 98 % of the azimuth errors and 80 % of the elevation errors remain below 5° in magnitude. This proves that, even in this worst-case scenario, a one-time anchor calibration is sufficient owing to the self-shielding characteristics of the proposed antenna array, which is highly desired in practical use cases. Measurements have also been performed in the three other quadrants. Similar results were obtained, confirming the estimation accuracy of the proposed 2×2 array over a wide field-of-view. In conclusion, these measurements show that the proposed 2×2 antenna array

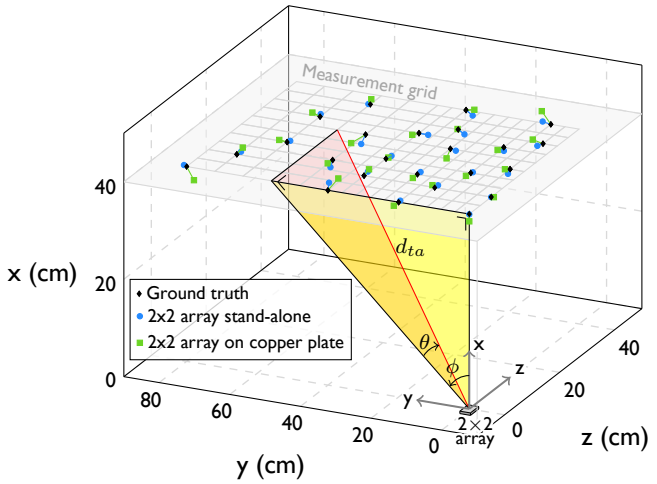

Fig. 13: Joint distance and 2D AoA estimation results: estimated grid positions in different measurement conditions (stand-alone array and array on copper plate), compared to the ground truth.

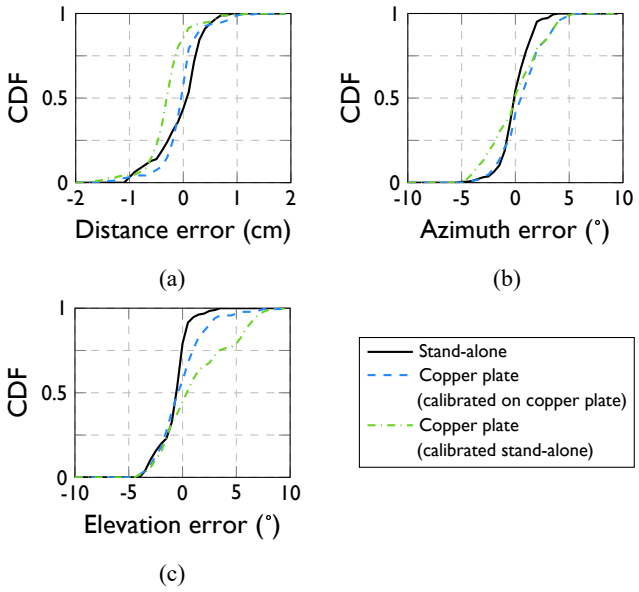

Fig. 14: Joint distance and AoA estimation errors in stand-alone conditions and with the anchor mounted on a copper plate: cumulative distribution functions (CDFs) of (a) distance errors, (b) azimuth angle errors and (c) elevation angle errors.

can be utilized as a multi-antenna anchor supporting accurate distance and 2D AoA estimation in both stand-alone conditions and when deployed on a copper plate.

D. Joint Distance and AoA Estimation Performance on a Vessel

A final measurement campaign is conducted to illustrate the joint distance and AoA estimation capabilities of the UWB multi-antenna system on a real-life vessel in an urban waterway setting with a limited amount of shore-side infrastructure. In this experiment, the vessel is navigating in a narrow canal in the city center of Ghent, Belgium, under a bridge, along a straight line parallel to the shore at a distance $d_s = 5.45$ m

with a constant velocity $v = 0.76\,\mathrm{m\,s^{-1}}$, as shown in Fig. 15a.

The vessel is equipped with an RTK-GNSS system, which can provide decimeter-level to centimeter-level accurate localization in ideal circumstances, depending on the base station locations and adopted post-processing methods [82], [83], and three IR-UWB anchor nodes, shown in detail in Fig. 15b. Each node consists of a 1×4 array prototype, with grounded co-planar waveguide (GCPW) feed lines, that is connected via vertical-mount SMA connectors and 90° SMA transition pieces to an IR-UWB hardware platform developed by Pozyx [84], containing four synchronized Qorvo DW1000 ICs [35]. A 1×4 array is selected because of its straightforward integration with the four-element hardware platform and the redundancy provided by the extra array elements. Leveraging a four-element array provides six possible antenna pairs for the computation of an AoA estimate, guaranteeing robustness against missing UWB frames and minimizing measurement errors. These three anchor nodes are placed in a waterproof housing and mounted on the metal railing of the vessel. On the shore side, a low-power low-complexity battery-powered UWB beacon node with a single antenna is deployed and transmitting UWB signals in channel 5. Based on these signals, the three anchor nodes each provide an AoA estimate for the azimuth angle φ using the PDoA algorithm. Based on these AoA estimates, the distance from the vessel to the shore d_s and the velocity of the vessel v is estimated in a subsequent step. By adopting this approach, the localization system's complexity is mainly incorporated on the vessel, and shore-side infrastructure is limited to small, low-cost and low-power UWB beacon nodes. While the current UWB beacon node is battery-powered, energy-harvesting components can be included to minimize maintenance cost and support fast cable-free deployment of the localization system in new areas.

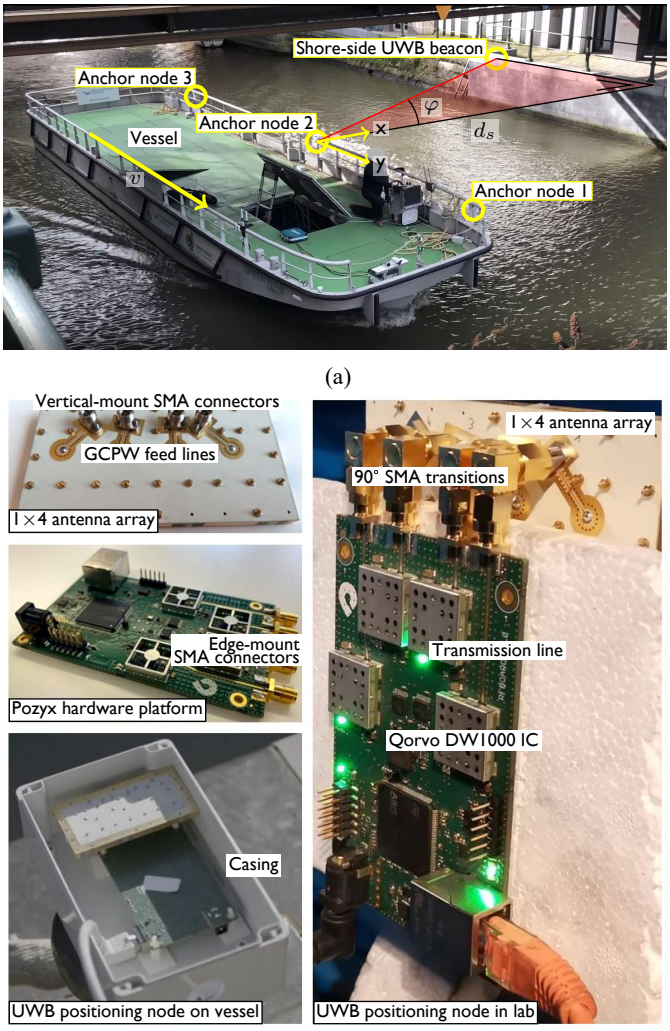

Fig. 15: Measurement campaign for distance and AoA estimation on a vessel: (a) three anchor nodes, deployed on the metal railing of the vessel, and (b) a detailed depiction of a UWB anchor node, consisting of a Pozyx hardware platform and a GCPW-fed 1×4 array. Each anchor node computes an AoA estimate for the azimuth angle φ (only indicated for anchor node 2), while the vessel is moving under a bridge.

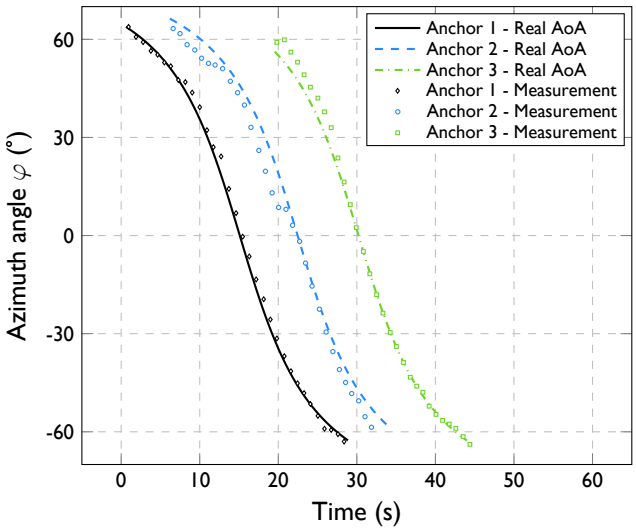

Fig. 16: Comparison of measured azimuth AoA estimates and the real azimuth angles-of-arrival on a moving vessel, for each of the three anchor nodes.

Fig. 16 shows the estimated azimuth angles (between −65° and 65°) for each of the three anchor nodes during the time interval in which the vessel is moving past the shore-side node. These are compared to the real azimuth angles-of-arrival, calculated by taking into account the vessel's trajectory and considering the known relative locations of the anchor nodes on the vessel. The ground truth for the vessel's trajectory is based on RTK-GNSS data. For that part of the trajectory where the vessel is navigating under the bridge and the RTK-GNSS system is unreliable, the ground truth is derived through dead-reckoning, assisted by logging the velocity and the heading of the vessel during the experiment. A good agreement is observed between the estimated and the calculated real azimuth angles. The maximum deviations for anchor one, two and three are 6.0°, 11.5° and 7.5°, respectively. In total, 96 % of AoA errors remain below 10°, and 83 % of errors remain below 5°. In the time interval where all three AoA estimates are available, the distance d_s and velocity v are estimated to be 5.40 m and

$0.78\,\mathrm{m\,s^{-1}}$, respectively. Hence, these results illustrate that the antenna element and array support accurate distance and AoA estimation, even in the challenging conditions encountered in urban shipping applications. Remark that while we only used one shore-side UWB beacon node in this setup, more beacon nodes can be deployed depending on the scenario and the required localization accuracy.

E. Comparison with State-of-the-Art

Table IV compares the proposed antenna to different state-of-the-art antenna elements and arrays, previously discussed in Section I-A, based on size, and frequency- and time-domain figures-of-merit. The proposed antenna exhibits best-in-class performance in terms of total efficiency η (incorporating radiation and matching losses), while providing a compact antenna footprint. Its excellent system-level time-domain performance is highlighted by a very high SFF and low GDV. Not listed in the table are its constant radiation pattern over the entire frequency range, large field-of-view (HPBW), low mutual coupling and low DEE. Furthermore, the cavity-backed antenna elements exhibit high robustness against integration platform effects and neighboring antenna elements and facilitate integration of active electronics on the backside of the cavity, minimizing the total system footprint.

TABLE IV:
STATE-OF-THE-ART ANTENNA COMPARISON

Ref.	Footprint [λ_c^3]	FBW [%]	η [%]	SFF [%]	GDV [ps]
[61]	0.54×0.54×0.03	133	> 63	-	< 1000
[65]	0.98×0.98×0.37	116	-	> 70	< 70
[63]	0.84×0.84×0.25	42.0	-	-	-
[71]	0.91×0.76×0.09	29.4	> 89	> 98	< 110
This	0.41×0.41×0.11	17.6	> 91	> 98.8	< 93

The measured impedance bandwidth is lower when compared to the state-of-the-art antennas in Table IV. However, these other works mainly focus on achieving a large bandwidth. In this article, the optimal trade-off is obtained between providing the bandwidth to cover channels 5 and 7 of the IEEE 802.15.4z standard, on the one hand, and introducing minimal orientation-specific pulse distortion after deployment in the actual application, on the other hand. Fig. 3 indicates that the proposed topology can reach a fractional bandwidth of over 30 % in a small footprint, but at the cost of significantly larger pulse distortion. The adopted optimization process yields an antenna that covers the necessary frequency range, while featuring excellent time-domain performance, which is the most critical requirement for accurate positioning. Compared to the PCB-based monopole antennas and DRAs, the proposed antenna sacrifices some bandwidth, while still fully covering channels 5 and 7, to guarantee robustness, high efficiency and minimal orientation-specific pulse distortion after being installed on its operational platform. Compared to the air-filled cavity-backed antenna, presented in [71], the proposed antenna sacrifices some bandwidth to obtain a more compact antenna element that fits in $\lambda/2$-spaced arrays.

Providing a straightforward and fair comparison in terms of AoA estimation performance is difficult. A large variety of chipsets, hardware platforms and antenna elements are used, but, more importantly, AoA estimates are computed differently throughout literature. Moreover, experiments are conducted in a wide range of scenarios and environments. In this article, the PDoA algorithm is adopted, which does not require significant post-processing, focusing on the raw performance of the proposed antenna (array). In contrast, most other works propose more elaborate and power-consuming algorithms to obtain accurate results. This is also done in our previous work [73] through machine learning techniques. Therefore, the summary presented in Table V focuses on the adopted chipsets and antenna topologies. It is clear that, typically, PCB-based and ceramic chip antennas are utilized in state-of-the-art UWB-based localization systems. Some works [36], [53] specifically state that better results can be obtained by using high-performance antennas. Yet, even though they exhibit several beneficial characteristics, in current literature, no AFSIW cavity-backed antenna element has been proposed yet for 2D AoA estimation systems.

TABLE V:
STATE-OF-THE-ART LOCALIZATION SYSTEMS COMPARISON

Ref.	IC	Antenna topology	AoA error [°] (pctl.)
[34]	Qorvo DW1000	PCB-based patch	8.25 (90^{th})
[35]	Qorvo DW1000	PCB-based monopole	< 10
[36]	NXP SR150	Ceramic chip	> 10
[37]	Qorvo DW3000	Ceramic chip	2.4 (50^{th})
[38]	Qorvo DW1000	Ceramic chip	< 20
[52]	Qorvo DW1000	PCB-based patch	< 10
[53]	Qorvo DW1000	Ceramic chip	4.15 (90^{th})
This	Qorvo DW1000	AFSIW cavity-backed	< 5 / 2.8 (99^{th}) [73]*

pctl.: percentile
*: our previous work (machine learning-based AoA estimation)

V. CONCLUSION

In this article, we have proposed a time-domain-optimized antenna array for joint distance and 2D angle-of-arrival (AoA) estimation based on the impulse-radio ultra-wideband (IR-UWB) technology to provide high-precision 3-dimensional (3D) localization of autonomous pallet shuttle barges (PSBs) in global navigation satellite system (GNSS)-denied critical waterway sections with minimal shore-side infrastructure. A three-step approach was adopted. First, we proposed a capacitively-coupled-fed guard-trace-based QM-AFSIW cavity-backed slot antenna. The quarter-mode miniaturization technique with guard trace inclusion and capacitively coupled feed provide an antenna element with wide bandwidth in a compact footprint that guarantees stable performance in the challenging urban shipping environments. A multi-objective system-level optimization process, focusing on frequency- and time-domain criteria, tailored the antenna towards IR-UWB-based joint distance and 2D AoA estimation. During the optimization process, the capacitive coupling

mechanism was exploited to simultaneously tune the magnitude of the antenna's input impedance for wideband matching and its phase to achieve low group delay variation. Extensive simulations indicated that the antenna retains its performance when embedded in scalable, planar 2D arrays. Frequency- and time-domain antenna measurements, with the antenna in free-space stand-alone conditions and when the antenna was mounted on a copper plate (mimicking the metal hull of a PSB), proved its stable performance when subjected to integration platform effects. Secondly, an extensive dedicated joint distance and 2D AoA estimation measurement campaign using a 2×2 array prototype was conducted, again in free-space stand-alone conditions and when the array was mounted on a copper plate. All distance errors stayed below 2 cm and all angular errors remained below 5° in stand-alone conditions. Finally, 1×4 array prototypes were incorporated in IR-UWB positioning nodes for deployment on a vessel. The results proved that the proposed antenna element is scalable to arrays in both dimensions, while exhibiting minimum susceptibility to its surroundings, such as neighboring elements and integration platforms. Additional localization experiments over large distances and in more complex environments may be included in future work. In conclusion, the proposed antenna element is excellently suited for adoption in multi-antenna IR-UWB localization systems to ensure reliable and high-accuracy 3D localization of a PSB in critical waterway sections, while relying on standard GNSS-based navigation during the largest part of its trajectory. This marks an important step towards the realization of more cost-effective autonomous PSBs, essential to accelerate the modal shift from conventional road-based transport to inland waterways.

REFERENCES

[1] R. I. Meneguette, R. E. De Grande, and A. A. F. Loureiro, *Intelligent Transport System in Smart Cities*. Springer International Publishing, 2018, ch. Intelligent Transportation Systems, pp. 1–21.

[2] J. K. Naufal *et al.*, "A2CPS: A Vehicle-Centric Safety Conceptual Framework for Autonomous Transport Systems," *IEEE Trans. Intell. Transp. Syst.*, vol. 19, pp. 1925–1939, 2018.

[3] C. Chen, Y. Zhang, M. R. Khosravi, Q. Pei, and S. Wan, "An Intelligent Platooning Algorithm for Sustainable Transportation Systems in Smart Cities," *IEEE Sens. J.*, vol. 21, pp. 15 437–15 447, 2021.

[4] H. Cao, S. Garg, G. Kaddoum, S. Singh, and M. S. Hossain, "Softwarized Resource Management and Allocation With Autonomous Awareness for 6G-Enabled Cooperative Intelligent Transportation Systems," *IEEE Trans. Intell. Transp. Syst.*, vol. 23, pp. 24 662–24 671, 2022.

[5] D. Darsena, G. Gelli, I. Iudice, and F. Verde, "Sensing Technologies for Crowd Management, Adaptation, and Information Dissemination in Public Transportation Systems: A Review," *IEEE Sensors J.*, vol. 23, no. 1, pp. 68–87, 2023.

[6] L. Chen, Y. Huang, H. Zheng, H. Hopman, and R. Negenborn, "Cooperative Multi-Vessel Systems in Urban Waterway Networks," *IEEE Trans. Intell. Transp. Syst.*, vol. 21, pp. 3294–3307, 2020.

[7] N. P. Reddy *et al.*, "Zero-Emission Autonomous Ferries for Urban Water Transport: Cheaper, Cleaner Alternative to Bridges and Manned Vessels," *IEEE Electrif. Mag.*, vol. 7, pp. 32–45, 2019.

[8] P. Shobayo, T. Vanelslander, and E. Van Hassel, "Socio-economic evaluation of palletized shuttle barges (PSBs) for urban freight delivery," *Int. J. Transp. Econ.*, pp. 525–550, 2021.

[9] M. Schiaretti, L. Chen, and R. R. Negenborn, "Survey on autonomous surface vessels: Part II-categorization of 60 prototypes and future applications," in *Proc. ICCL*, Southampton, UK, 2017, pp. 234–252.

[10] U. Öztürk, M. Akdağ, and T. Ayabakan, "A Review of Path Planning Algorithms in Maritime Autonomous Surface Ships: Navigation Safety Perspective," *Ocean Eng.*, vol. 251, p. 111010, 2022.

[11] X. Zhang, C. Wang, L. Jiang, L. An, and R. Yang, "Collision-Avoidance Navigation Systems for Maritime Autonomous Surface Ships: A State of the Art Survey," *Ocean Eng.*, vol. 235, p. 109380, 2021.

[12] Z. Peng, J. Wang, D. Wang, and Q.-L. Han, "An Overview of Recent Advances in Coordinated Control of Multiple Autonomous Surface Vehicles," *IEEE Trans. Ind. Informat.*, vol. 17, no. 2, pp. 732–745, 2021.

[13] D. K. M. Kufoalor, T. A. Johansen, E. F. Brekke, A. Hepsø, and K. Trnka, "Autonomous Maritime Collision Avoidance: Field Verification of Autonomous Surface Vehicle Behavior in Challenging Scenarios," *Journal of Field Robotics*, vol. 37, no. 3, pp. 387–403, 2020.

[14] E. F. Brekke *et al.*, "milliAmpere: An Autonomous Ferry Prototype," *Journal of Physics: Conference Series*, vol. 2311, no. 1, jul 2022.

[15] J. Lin *et al.*, "Environment Perception and Object Tracking for Autonomous Vehicles in a Harbor Scenario," in *Proc. IEEE ITSC*, 2020, pp. 1–6.

[16] A. B. Martinsen, G. Bitar, A. M. Lekkas, and S. Gros, "Optimization-Based Automatic Docking and Berthing of ASVs Using Exteroceptive Sensors: Theory and Experiments," *IEEE Access*, vol. 8, pp. 204 974–204 986, 2020.

[17] F. T. El-Hassan, "Experimenting With Sensors of a Low-Cost Prototype of an Autonomous Vehicle," *IEEE Sens. J.*, vol. 20, pp. 13 131–13 138, 2020.

[18] S. A. S. Mohamed *et al.*, "A Survey on Odometry for Autonomous Navigation Systems," *IEEE Access*, vol. 7, pp. 97 466–97 486, 2019.

[19] H.-F. Ng, G. Zhang, and L.-T. Hsu, "Robust GNSS Shadow Matching for Smartphones in Urban Canyons," *IEEE Sens. J.*, vol. 21, pp. 18 307–18 317, 2021.

[20] H. H. Helgesen *et al.*, "Inertial Navigation Aided by Ultra-Wideband Ranging for Ship Docking and Harbor Maneuvering," *IEEE J. Ocean. Eng.*, vol. 48, no. 1, pp. 27–42, 2023.

[21] B. Hu, X. Liu, Q. Jing, H. Lyu, and Y. Yin, "Estimation of Berthing State of Maritime Autonomous Surface Ships Based on 3D LiDAR," *Ocean Eng.*, vol. 251, p. 111131, 2022.

[22] K. N. Lwin *et al.*, "Visual Docking Against Bubble Noise With 3-D Perception Using Dual-Eye Cameras," *IEEE J. Ocean. Eng.*, vol. 45, no. 1, pp. 247–270, 2020.

[23] A. Alarifi *et al.*, "Ultra Wideband Indoor Positioning Technologies: Analysis and Recent Advances," *Sensors*, vol. 16, no. 5, 2016.

[24] M. Elsanhoury *et al.*, "Precision Positioning for Smart Logistics Using Ultra-Wideband Technology-Based Indoor Navigation: A Review," *IEEE Access*, vol. 10, pp. 44 413–44 445, 2022.

[25] U.-S. Suh, G. Lee, J. Han, T. W. Kim, and W.-S. Ra, "Passive IR-UWB Localization System for UAV-Based Electric Facility Inspection During GPS Outage," *IEEE Access*, vol. 11, pp. 39 597–39 608, 2023.

[26] K. Guo, X. Li, and L. Xie, "Ultra-Wideband and Odometry-Based Cooperative Relative Localization With Application to Multi-UAV Formation Control," *IEEE Trans. Cybern.*, vol. 50, no. 6, pp. 2590–2603, 2020.

[27] D. Dardari, A. Conti, U. Ferner, A. Giorgetti, and M. Z. Win, "Ranging With Ultrawide Bandwidth Signals in Multipath Environments," *Proc. IEEE*, vol. 97, no. 2, pp. 404–426, 2009.

[28] B. Van Herbruggen *et al.*, "Wi-PoS: A Low-Cost, Open Source Ultra-Wideband (UWB) Hardware Platform with Long Range Sub-GHz Backbone," *Sensors*, vol. 19, no. 7, p. 1548, 2019.

[29] M. Martalò *et al.*, "Improved UWB TDoA-Based Positioning Using a Single Hotspot for Industrial IoT Applications," *IEEE Trans. Ind. Informat.*, vol. 18, no. 6, pp. 3915–3925, 2022.

[30] Y.-Y. Li, G.-Q. Qi, and A.-D. Sheng, "Performance Metric on the Best Achievable Accuracy for Hybrid TOA/AOA Target Localization," *IEEE Commun. Lett.*, vol. 22, no. 7, pp. 1474–1477, 2018.

[31] H. Wymeersch, J. Lien, and M. Z. Win, "Cooperative Localization in Wireless Networks," *Proc. IEEE*, vol. 97, no. 2, pp. 427–450, 2009.

[32] F. Shang, B. Champagne, and I. N. Psaromiligkos, "A ML-Based Framework for Joint TOA/AOA Estimation of UWB Pulses in Dense Multipath Environments," *IEEE Trans. Wireless Commun.*, vol. 13, no. 10, pp. 5305–5318, 2014.

[33] L. Taponecco, A. D'Amico, and U. Mengali, "Joint TOA and AOA Estimation for UWB Localization Applications," *IEEE Trans. Wireless Commun.*, vol. 10, no. 7, pp. 2207–2217, 2011.

[34] M. Heydariaan, H. Dabirian, and O. Gnawali, "AnguLoc: Concurrent Angle of Arrival Estimation for Indoor Localization with UWB Radios," in *Proc. IEEE DCOSS*, 2020, pp. 112–119.

[35] I. Dotlic, A. Connell, H. Ma, J. Clancy, and M. McLaughlin, "Angle of Arrival Estimation Using Decawave DW1000 Integrated Circuits," in *Proc. IEEE WPNC*, 2017, pp. 1–6.

[36] R. Juran *et al.*, "Hands-On Experience with UWB: Angle of Arrival Accuracy Evaluation in Channel 9," in *Proc. IEEE ICUMT*, Valencia, Spain, 2022, pp. 45–49.

[37] T. Margiani *et al.*, "Angle of Arrival and Centimeter Distance Estimation on a Smart UWB Sensor Node," *IEEE Trans. Instrum. Meas.*, pp. 1–1, 2023.

[38] J. Tiemann, O. Fuhr, and C. Wietfeld, "CELIDON: Supporting First Responders through 3D AOA-based UWB Ad-Hoc Localization," in *Proc. IEEE WiMob*, 2020, pp. 20–25.

[39] W. Wiesbeck, G. Adamiuk, and C. Sturm, "Basic Properties and Design Principles of UWB Antennas," *Proc. IEEE*, vol. 97, no. 2, pp. 372–385, 2009.

[40] V. Sipal, M. John, D. Neirynck, M. McLaughlin, and M. Ammann, "Advent of Practical UWB Localization: (R)Evolution in UWB Antenna Research," in *Proc. 8th Eur. Conf. Antennas Propag. (EuCAP)*, The Hague, The Netherlands, 2014, pp. 1561–1565.

[41] D.-H. Kwon, "Effect of Antenna Gain and Group Delay Variations on Pulse-Preserving Capabilities of Ultrawideband Antennas," *IEEE Trans. Antennas Propag.*, vol. 54, no. 8, pp. 2208–2215, 2006.

[42] Q. V. d. Brande, S. Lemey, and H. Rogier, "Planar Sectoral Antenna for IR-UWB Localization with Minimal Range Estimation Biasing," *IEEE Antennas Wireless Propag. Lett.*, vol. 20, no. 2, pp. 135–139, 2021.

[43] A. D. Preter, G. Goysens, J. Anthonis, J. Swevers, and G. Pipeleers, "Range Bias Modeling and Autocalibration of an UWB Positioning System," in *Proc. IEEE IPIN*, Pisa, Italy, 2019, pp. 1–8.

[44] B. Silva and G. P. Hancke, "IR-UWB-Based Non-Line-of-Sight Identification in Harsh Environments: Principles and Challenges," *IEEE Trans. Ind. Informat.*, vol. 12, no. 3, pp. 1188–1195, 2016.

[45] A. Celik, K. N. Salama, and A. M. Eltawil, "The Internet of Bodies: A Systematic Survey on Propagation Characterization and Channel Modeling," *IEEE Internet Things J.*, vol. 9, no. 1, pp. 321–345, 2022.

[46] Y. He *et al.*, "A Novel 3D Non-Stationary Maritime Wireless Channel Model," *IEEE Trans. Commun.*, vol. 70, no. 3, pp. 2102–2116, 2022.

[47] M. Švecová *et al.*, "Through-the-Floor Localization of a Static Person by a Multistatic UWB Radar," *Microw. Opt. Technol. Lett.*, vol. 61, no. 3, pp. 825–831, 2019.

[48] A. E.-C. Tan, M. Y.-W. Chia, and K. Rambabu, "Time Domain Characterization of Circularly Polarized Ultrawideband Array," *IEEE Trans. Antennas Propag.*, vol. 58, no. 11, pp. 3524–3531, 2010.

[49] M. Islam, M. Mahmud, M. T. Islam, S. Kibria, and M. Samsuzzaman, "A Low Cost and Portable Microwave Imaging System for Breast Tumor Detection Using UWB Directional Antenna Array," *Sci. Rep.*, vol. 9, no. 1, pp. 1–13, 2019.

[50] C.-H. Liao, P. Hsu, and D.-C. Chang, "Energy Patterns of UWB Antenna Arrays With Scan Capability," *IEEE Trans. Antennas Propag.*, vol. 59, no. 4, pp. 1140–1147, 2011.

[51] M. A. Hussain Ansari and C. L. Law, "Grating Lobe Suppression of Multicycle IR-UWB Collaborative Radar Sensor in Wireless Sensor Network System," *IEEE Sens. Lett.*, vol. 4, no. 1, pp. 1–4, 2020.

[52] S. Diagne, T. Val, A. K. Farota, B. Diop, and O. Assogba, "Performances Analysis of a System of Localization by Angle of Arrival UWB Radio," *Int. J. Comm. Netw. System Sci.*, vol. 13, no. 2, pp. 15–27, 2020.

[53] M. Zhao *et al.*, "ULoc: Low-Power, Scalable and cm-Accurate UWB-Tag Localization and Tracking for Indoor Applications," *Proc. ACM Interactive Mobile Wearable Ubiquitous Technol.*, vol. 5, no. 3, pp. 1–31, 2021.

[54] J. T. Logan, W. M. Dorsey, and J. A. Valenzi, "Modular All-Metal Ultrawideband Cylindrical Array for Multifunction Operation," *IEEE Trans. Antennas Propag.*, vol. 70, no. 10, pp. 9175–9183, 2022.

[55] Z. Jiang, S. Xiao, Z. Yao, and B.-Z. Wang, "A Planar Ultrawideband Wide-Angle Scanning Array Loaded with Polarization-Sensitive Frequency-Selective Surface Structure," *IEEE Trans. Antennas Propag.*, vol. 68, no. 11, pp. 7348–7357, 2020.

[56] R. W. Kindt and B. T. Binder, "Dual-Polarized Planar-Printed Ultrawideband Antenna Array on a Triangular Grid," *IEEE Trans. Antennas Propag.*, vol. 68, no. 8, pp. 6136–6144, 2020.

[57] S. R. Emadian, J. Ahmadi-Shokouh, C. Ghobadi, and J. Nourinia, "Study on Frequency and Impulse Response of Novel Triple Band Notched UWB Antenna in Indoor Environments," *Int. J. Electron. Commun.*, vol. 96, pp. 93–106, 2018.

[58] *DW1000 Hardware Design Guide (Application Note APH001)*, Qorvo, 2018, rev. 1.1. [Online]. Available: https://www.qorvo.com/products/p/DW1000#documents

[59] Z. Lasemiimeni, Z. Atlasbaf, and N. Karbaschi, "Dual-Functional Ultrawideband Antenna with High Fidelity Factor for Body Area Networks and Microwave Imaging Systems," *IEEE Access*, vol. 9, pp. 112 930–112 941, 2021.

[60] W. He, Y. He, Y. Li, S.-W. Wong, and L. Zhu, "A Compact Ultrawideband Circularly Polarized Antenna Array With Shared Partial Patches," *IEEE Antennas Wireless Propag. Lett.*, vol. 20, no. 12, pp. 2280–2284, 2021.

[61] D. Sipal, M. P. Abegaonkar, and S. K. Koul, "Easily Extendable Compact Planar UWB MIMO Antenna Array," *IEEE Antennas Wireless Propag. Lett.*, vol. 16, pp. 2328–2331, 2017.

[62] M. R. Nikkhah, A. A. Kishk, and J. Rashed-Mohassel, "Wideband DRA Array Placed on Array of Slot Windows," *IEEE Trans. Antennas Propag.*, vol. 63, no. 12, pp. 5382–5390, 2015.

[63] F. Abushakra, A. Al-Zoubi, I. Al-Hmoud, T. Walpita, and N. Jeong, "Wideband and High Efficiency 64-Element RDRA Array for Radar Applications," *IEEE Open J. Antennas Propag.*, vol. 2, pp. 932–936, 2021.

[64] A. Bhattacharya, B. Dasgupta, and R. Jyoti, "Performance Analysis of a Hybrid Dielectric Resonator Antenna in Frequency and Time Domains," *Int. J. RF Microw. Comput. Aided Eng.*, vol. 29, no. 10, p. e21886, 2019.

[65] M. Shahzad Iqbal and K. P. Esselle, "Pulse-Preserving Characteristics and Effective Isotropically Radiated Power Spectra of a New Ultrawideband Dielectric Resonator Antenna," *IET Microw. Antennas Propag.*, vol. 12, no. 7, pp. 1231–1238, 2018.

[66] A. Reyna, M. A. Panduro, A. L. Méndez, and G. Romero, "Timed Arrays of Spiral Antennas for Circularly Polarised UWB Scanned Patterns with Low Side Lobes," *IET Microw. Antennas Propag.*, vol. 10, no. 5, pp. 587–593, 2016.

[67] D. Van Baelen *et al.*, "Fully Flexible Textile Antenna-Backed Sensor Node for Body-Worn UWB Localization," *Sensors*, vol. 21, no. 5, p. 1641, 2021.

[68] K. Y. Kapusuz *et al.*, "Polarization Reconfigurable Air-Filled Substrate Integrated Waveguide Cavity-Backed Slot Antenna," *IEEE Access*, vol. 7, pp. 102 628–102 643, 2019.

[69] I. Lima de Paula *et al.*, "Cost-Effective High-Performance Air-Filled SIW Antenna Array for the Global 5G 26 GHz and 28 GHz Bands," *IEEE Antennas Wireless Propag. Lett.*, vol. 20, no. 2, pp. 194–198, 2021.

[70] N. Claus, J. Verhaevert, and H. Rogier, "High-Performance Air-Filled Multiband Antenna for Seamless Integration Into Smart Surfaces," *IEEE Antennas Wireless Propag. Lett.*, vol. 20, no. 12, pp. 2260–2264, 2021.

[71] Q. Van den Brande, S. Lemey, J. Vanfleteren, and H. Rogier, "Highly Efficient Impulse-Radio Ultra-Wideband Cavity-Backed Slot Antenna in Stacked Air-Filled Substrate Integrated Waveguide Technology," *IEEE Trans. Antennas Propag.*, vol. 66, no. 5, pp. 2199–2209, 2018.

[72] G. Singh *et al.*, "An IR-UWB IEEE 802.15.4z Compatible Coherent Asynchronous Polar Transmitter in 28-nm CMOS," *IEEE J. Solid-State Circuits*, vol. 56, no. 12, pp. 3799–3810, 2021.

[73] M. Naseri *et al.*, "Machine Learning-Based Angle of Arrival Estimation for Ultra-Wide Band Radios," *IEEE Commun. Lett.*, vol. 26, no. 6, pp. 1273–1277, 2022.

[74] "IEEE Standard for Low-Rate Wireless Networks," *IEEE Std 802.15.4-2020 (Revision of IEEE Std 802.15.4-2015)*, pp. 1–800, 2020.

[75] "IEEE Standard for Low-Rate Wireless Networks–Amendment 1: Enhanced Ultra Wideband (UWB) Physical Layers (PHYs) and Associated Ranging Techniques," *IEEE Std 802.15.4z-2020 (Amendment to IEEE Std 802.15.4-2020)*, pp. 1–174, 2020.

[76] G. Quintero, J.-F. Zurcher, and A. K. Skrivervik, "System Fidelity Factor: A New Method for Comparing UWB Antennas," *IEEE Trans. Antennas Propag.*, vol. 59, no. 7, pp. 2502–2512, 2011.

[77] S. Agneessens, S. Lemey, T. Vervust, and H. Rogier, "Wearable, Small, and Robust: The Circular Quarter-Mode Textile Antenna," *IEEE Antennas Wireless Propag. Lett.*, vol. 14, pp. 1482–1485, 2015.

[78] S. Radavaram and M. Pour, "A Wideband Coplanar L-Strip Fed Rectangular Patch Antenna," *IEEE Antennas Wireless Propag. Lett.*, vol. 20, no. 9, pp. 1779–1783, 2021.

[79] T. Latha, G. Ram, G. A. Kumar, and M. Chakravarthy, "Review on Ultra-Wideband Phased Array Antennas," *IEEE Access*, vol. 9, pp. 129 742–129 755, 2021.

[80] *ADRF5046, Silicon SP4T Switch, Reflective, 100 MHz to 44 GHz*, Analog Devices, 2019, rev. 0, datasheet.

[81] H. L. Van Trees, *Optimum array processing: Part IV of detection, estimation, and modulation theory*. John Wiley & Sons, 2004.

[82] X. Yan *et al.*, "Performance Analysis of Oceanographic Research Vessel Precise Point Positioning Based on BDS/GNSS RTK Receivers," *Measurement*, vol. 211, p. 112637, 2023.

[83] Y. Zhu, F. Ming, X. Cui, C. Cai, and X. Jia, "Performance Analysis of BDS-3 Vehicle-/Ship-/Air-Borne Kinematic SPP/PPP/RTK," *Advances in Space Research*, 2023.

[84] Pozyx. [Online]. Available: https://www.pozyx.io/products/hardware/